

BEACON: JWST NIRCam Pure-parallel Imaging Survey. I. Survey Design and Initial Results

TAKAHIRO MORISHITA ^{1,*} CHARLOTTE A. MASON ^{2,3,*} KIMI C. KREILGAARD ^{2,3} MICHELE TRENTI ^{4,5}
TOMMASO TREU ⁶ BENEDETTA VULCANI ⁷ YECI ZHANG ¹ ABDURRO'UF ^{8,9} ANAHITA ALAVI ¹⁰
HAKIM ATEK ¹¹ YANNICK BAHÉ ¹² MARUŠA BRADAČ ^{13,14} LARRY D. BRADLEY ⁹ ANDREW J. BUNKER ¹⁵
DAN COE ^{9,16,8} JAMES COLBERT ¹⁷ VIOLA GELLI ^{2,3} MATTHEW J. HAYES ¹⁸ TUCKER JONES ¹⁹
TADAYUKI KODAMA ²⁰ NICHA LEETHOCHAWALIT ²¹ ZHAORAN LIU ²⁰ MATTHEW A. MALKAN ²²
VIHANG MEHTA ¹⁷ BENJAMIN METHA ^{4,5} ANDREW B. NEWMAN ²³ MARC RAFELSKI ^{24,25}
GUIDO ROBERTS-BORSANI ²⁶ MICHAEL J. RUTKOWSKI ²⁷ CLAUDIA SCARLATA ²⁸ MASSIMO STIAVELLI ²⁹
RYO A. SUTANTO ²⁰ KOSUKE TAKAHASHI ²⁰ HARRY I. TEPLITZ ¹⁰ AND XIN WANG ^{30,31,32}

¹IPAC, California Institute of Technology, MC 314-6, 1200 E. California Boulevard, Pasadena, CA 91125, USA

²Cosmic Dawn Center (DAWN)

³Niels Bohr Institute, University of Copenhagen, Jagtvej 128, DK-2200 Copenhagen N, Denmark

⁴School of Physics, University of Melbourne, Parkville 3010, VIC, Australia

⁵ARC Centre of Excellence for All Sky Astrophysics in 3 Dimensions (ASTRO 3D), Australia

⁶Department of Physics and Astronomy, University of California, Los Angeles, 430 Portola Plaza, Los Angeles, CA 90095, USA

⁷INAF Osservatorio Astronomico di Padova, vicolo dell'Osservatorio 5, 35122 Padova, Italy

⁸Department of Physics and Astronomy, The Johns Hopkins University, 3400 N Charles St. Baltimore, MD 21218, USA

⁹Space Telescope Science Institute (STScI), 3700 San Martin Drive, Baltimore, MD 21218, USA

¹⁰IPAC, Mail Code 314-6, California Institute of Technology, 1200 E. California Blvd., Pasadena CA, 91125, USA

¹¹Institut d'Astrophysique de Paris, CNRS, Sorbonne Université, 98bis Boulevard Arago, 75014, Paris, France

¹²Institute of Physics, Laboratory of Astrophysics, Ecole Polytechnique Fédérale de Lausanne (EPFL), Observatoire de Sauverny, CH-1290 Versoix, Switzerland

¹³University of Ljubljana, Department of Mathematics and Physics, Jadranska ulica 19, SI-1000 Ljubljana, Slovenia

¹⁴Department of Physics and Astronomy, University of California Davis, 1 Shields Avenue, Davis, CA 95616, USA

¹⁵Department of Physics, University of Oxford, Denys Wilkinson Building, Keble Road, Oxford OX1 3RH, UK

¹⁶Association of Universities for Research in Astronomy (AURA), Inc. for the European Space Agency (ESA)

¹⁷IPAC, California Institute of Technology, 1200 E. California Blvd, Pasadena, CA 91125, USA

¹⁸Stockholm University, Department of Astronomy and Oskar Klein Centre for Cosmoparticle Physics, AlbaNova University Centre, SE-10691, Stockholm, Sweden.

¹⁹University of California, Davis, Department of Physics and Astronomy, One Shields Avenue, Davis, CA 95616, USA

²⁰Astronomical Institute, Tohoku University, 6-3 Aramaki, Aoba-ku, Sendai 980-8578, Japan

²¹National Astronomical Research Institute of Thailand (NARIT), Mae Rim, Chiang Mai, 50180, Thailand

²²University of California, Los Angeles, Department of Physics and Astronomy, 430 Portola Plaza, Los Angeles, CA 90095, USA

²³Observatories of the Carnegie Institution for Science, Pasadena, CA, USA

²⁴Space Telescope Science Institute, 3700 San Martin Drive, Baltimore, MD, 21218 USA

²⁵Department of Physics and Astronomy, Johns Hopkins University, Baltimore, MD 21218, USA

²⁶Department of Astronomy, University of Geneva, Chemin Pegasi 51, 1290 Versoix, Switzerland

²⁷Minnesota State University, Mankato, Department of Physics and Astronomy, 141 Trafton Science Center N, Mankato, MN 56001, USA

²⁸University of Minnesota, Twin Cities, 116 Church St SE, Minneapolis, MN 55455, USA

²⁹Space Telescope Science Institute, 3700 San Martin Drive, Baltimore, MD 21218, USA

³⁰School of Astronomy and Space Science, University of Chinese Academy of Sciences (UCAS), Beijing 100049, China

³¹National Astronomical Observatories, Chinese Academy of Sciences, Beijing 100101, China

³²Institute for Frontiers in Astronomy and Astrophysics, Beijing Normal University, Beijing 102206, China

Submitted to ApJ

ABSTRACT

We introduce the Bias-free Extragalactic Analysis for Cosmic Origins with NIRCam (BEACON) survey, a JWST Cycle 2 program allocated up to 600 *pure-parallel* hours of observations. BEACON explores high-latitude areas of the sky with JWST/NIRCam over ~ 100 independent sightlines, totaling $\sim 0.3 \text{ deg}^2$, reaching a median F444W depth of ≈ 28.2 AB mag (5σ). Based on existing JWST observations in legacy fields, we estimate that BEACON will photometrically identify 25–150 galaxies at $z > 10$ and 500–1000 at $z \sim 7$ –10 uniquely enabled by an efficient multiple filter configuration spanning 0.9 – $5.0 \mu\text{m}$. The expected sample size of $z > 10$ galaxies will allow us to obtain robust number density estimates and to discriminate between different models of early star formation. In this paper, we present an overview of the survey design and initial results using the first 19 fields. We present 129 galaxy candidates at $z \gtrsim 7$ identified in those fields, including 11 galaxies at $z \gtrsim 10$ and several UV-luminous ($M_{\text{UV}} < -21$ mag) galaxies at $z \sim 8$. The number densities of $z < 13$ galaxies inferred from the initial fields are overall consistent with those in the literature. Despite reaching a considerably large volume ($\sim 10^5 \text{ Mpc}^3$), however, we find no galaxy candidates at $z > 13$, providing us with a complimentary insight into early galaxy evolution with minimal cosmic variance. We publish imaging and catalog data products for these initial fields. Upon survey completion, all BEACON data will be coherently processed and distributed to the community along with catalogs for redshift and other physical quantities.

Keywords: Galaxies (573) — High-redshift galaxies (734) — Reionization (1383)

1. INTRODUCTION

Space telescopes have been essential for understanding galaxy formation and evolution, with the Hubble Space Telescope (HST) in particular progressively extending our frontiers from the pioneering Hubble Deep Field at redshift $z \sim 4$ (lookback time ~ 12 Gyr; e.g., Madau et al. 1996), to more recent discoveries of galaxies in the epoch of reionization (EoR, $z \sim 6$ –10, lookback time > 13 Gyr; e.g., Bunker et al. 2004; Oesch et al. 2010; Bouwens et al. 2010; Bunker et al. 2010; Ellis et al. 2013; Bouwens et al. 2015; Oesch et al. 2018; Ishigaki et al. 2018). However, even with the deepest HST and Spitzer data, key questions remained unanswered: When and how did the first sources of light form? How was intergalactic hydrogen reionized? How are galaxy mass and structure acquired across cosmic time? The James Webb Space Telescope (JWST) was designed to address these fundamental questions.

JWST Cycle 1 was a watershed moment. It extended the frontier of galaxy detection to the first 400 million years after the Big Bang ($z \gtrsim 11$) during the initial stages of reionization, finding a tantalizingly high abundance of bright, potentially massive galaxy candidates, unanticipated by theoretical models (e.g., Castellano et al. 2022; Naidu et al. 2022; Donnan et al. 2022; Curtis-Lake et al. 2022; Finkelstein et al. 2022; Carniani et al. 2024). Furthermore, the observed number of massive quenched

galaxies exceeds expectations across $z \sim 3$ –9 (Carnall et al. 2022; de Graaff et al. 2024; Glazebrook et al. 2024; Nanayakkara et al. 2024), a number of low-luminosity and dusty quasars (Onoue et al. 2023; Harikane et al. 2023b; Matthee et al. 2023; Kocevski et al. 2023) or active galactic nuclei (AGN)-galaxy complexes (Übler et al. 2023; Larson et al. 2023; Scholtz et al. 2023; Greene et al. 2023) have been revealed, and some galaxies seem to already have (proto-) disk structures (Ferreira et al. 2022; Fudamoto et al. 2022; Guo et al. 2022). However, these early results have come from just a handful of small public legacy fields (e.g., McLeod et al. 2024), leaving open the question of how representative they are of the entire early Universe. More recently, Willott et al. (2024) extended the analysis to five new fields and found no luminous galaxies at $z > 10$, a stark contrast to the early studies.

Luminous galaxies are rare ($< 10^{-5} \text{ Mpc}^{-3}$ for $M_{\text{UV}} < -21$ at $z > 7$; Bouwens et al. 2015) and inevitably subject to cosmic variance (Somerville et al. 2004; Trenti & Stiavelli 2008; Robertson 2010; Bhowmick et al. 2020). A good example of strong cosmic variance is that Roberts-Borsani et al. (2016) discovered three bright ($m_{\text{AB}} < 26$) $z > 7$ galaxy candidates in just one of the five CANDELS fields, EGS, whereas only one comparably bright candidate was detected from the other four fields. Subsequent follow-up in EGS with HST, ground-based spectroscopy, and JWST has revealed that this region appears overdense at $z \sim 7$ –9, and contains the majority of Lyman- α emission detected across all

* These authors equally contributed to this work.

legacy fields at $z > 7$, likely pointing to a site of significant star formation that reionized early (Stark et al. 2017; Tilvi et al. 2020; Larson et al. 2022; Jung et al. 2022; Tang et al. 2023; Chen et al. 2023; Whitler et al. 2023). Such examples clearly demonstrate that a survey of many sightlines, as a supplement to legacy-type surveys with a small number of sightlines, is necessary for unbiased measurements in the early Universe.

Pure-parallel observations offer an ideal opportunity to meet this requirement. While the primary instrument is in operation, a secondary instrument can be used in parallel to observe a field a few arc-minutes away. Since the coordinates of the pure-parallel field cannot be specified, pure-parallel opportunities are often used to identify objects without any prior knowledge, minimizing the effects of cosmic variance (Fig. 1; also Atek et al. 2011; Trapp et al. 2022).

Starting in 2010, there have been several such HST pure-parallel programs (see Morishita et al. 2020 for a review). For example, the BoRG program (Trenti et al. 2011), which consisted of > 1000 HST orbits collected through multiple HST Cycles, successfully identified $z \sim 8\text{--}11$ galaxy candidates at the bright-end magnitude range, $M_{\text{UV}} \sim -21$ to -23 mag (Trenti et al. 2012; Bradley et al. 2012; Schmidt et al. 2014; Calvi et al. 2016; Bernard et al. 2016; Morishita et al. 2018, 2020). Identification of such luminous sources from a sufficiently large volume is critical to determine the shape of the luminosity function and its evolution with minimal cosmic variance (Bowler et al. 2014, 2020; Bouwens et al. 2015; Livermore et al. 2018; Bridge et al. 2019; Ren et al. 2019; Rojas-Ruiz et al. 2020; Leethochawalit et al. 2023).

The unexpected detection of many luminous $z > 10$ galaxies with JWST demonstrates one reason that pure-parallel efforts are crucial to continue in the era of JWST. Pure-parallel imaging with NIRCam is ideally suited to robustly identify $z > 10$ galaxies and to characterize the shape of UV luminosity functions. Surveying many independent sightlines samples the Universe in an unbiased way and enables studies of galaxy evolution as a function of a wide range of environments (see also Williams et al. 2024, for their Cycle 1 NIRCam Pure-parallel imaging program, PANORAMIC).

In addition, the pure-parallel mode is essentially at no cost in JWST primary observing time, thus enhancing current and planned programs in legacy fields. Thanks to the dichroic blue and red channels, pure-parallel imaging with NIRCam surveys are twice as efficient as on HST, and uniquely sample wavelengths of $> 2\,\mu\text{m}$ which is inaccessible to wider-area optical – near-IR missions like Euclid and Roman.

Identified bright galaxies are ideal targets for follow-up spectroscopy from ground-based facilities (Treu et al. 2013; Morishita et al. 2020; Roberts-Borsani et al. 2022) and now with JWST. Early NIRSpec follow-up on previously identified HST Borg sources confirmed 10 sources with < 1 hr exposure times (Roberts-Borsani et al. 2024a; Rojas-Ruiz et al. 2024). However, the low-redshift contamination rate among these HST-selected sources was significant – in the range $\sim 20\text{--}50\%$ depending on redshift, depth of observations and available bands bluewards of the Lyman break (Leethochawalit et al. 2023). This was expected (e.g., Vulcani et al. 2017), and largely attributable to the small number of HST filters up to $1.6\,\mu\text{m}$ (i.e., rest-frame $> 2000\,\text{\AA}$ at $z > 8$) and the lack of sensitive constraints at longer wavelengths that cover rest-frame optical. Multi-band JWST NIRCam imaging greatly improves our ability to obtain robust $z > 8$ galaxy samples with a much lower low- z interloper fraction (e.g., Morishita & Stiavelli 2023).

Here, we introduce Bias-free Extragalactic Analysis for Cosmic Origins with NIRCam (BEACON), a new JWST pure-parallel imaging survey approved for 600 pure-parallel hours in Cycle 2. BEACON is optimized to detect $z > 7.3$ Lyman-break galaxies, but also is capable of identifying lower redshift galaxies with up to 8-filter imaging. By surveying ~ 100 high-latitude blank fields (equivalent to $\sim 0.3\,\text{deg}^2$), it will allow the identification of galaxies over a wide redshift range.

In this overview paper, we present the survey design and initial highlights from the first 19 observed fields. Dedicated studies of UV luminosity functions and galaxy properties will be presented in forthcoming papers (Kreilgaard, in prep.; Zhang, in prep.). In Sec. 2, we outline the science goals of our program. We present the observing configurations and data reduction in Sec. 3, followed by photometric analysis of the initial fields in Sec. 4. We release the initial dataset on a dedicated webpage¹.

Where relevant, we adopt the AB magnitude system (Oke & Gunn 1983; Fukugita et al. 1996), cosmological parameters of $\Omega_m = 0.3$, $\Omega_\Lambda = 0.7$, $H_0 = 70\,\text{km s}^{-1}\,\text{Mpc}^{-1}$, and the Chabrier (2003) initial mass function (IMF).

2. SURVEY GOALS

BEACON takes advantage of the unique pure-parallel opportunity provided by the observatory to obtain $1\text{--}5\,\mu\text{m}$ NIRCam imaging over ~ 100 independent point-

¹ <https://beacon-jwst.github.io>

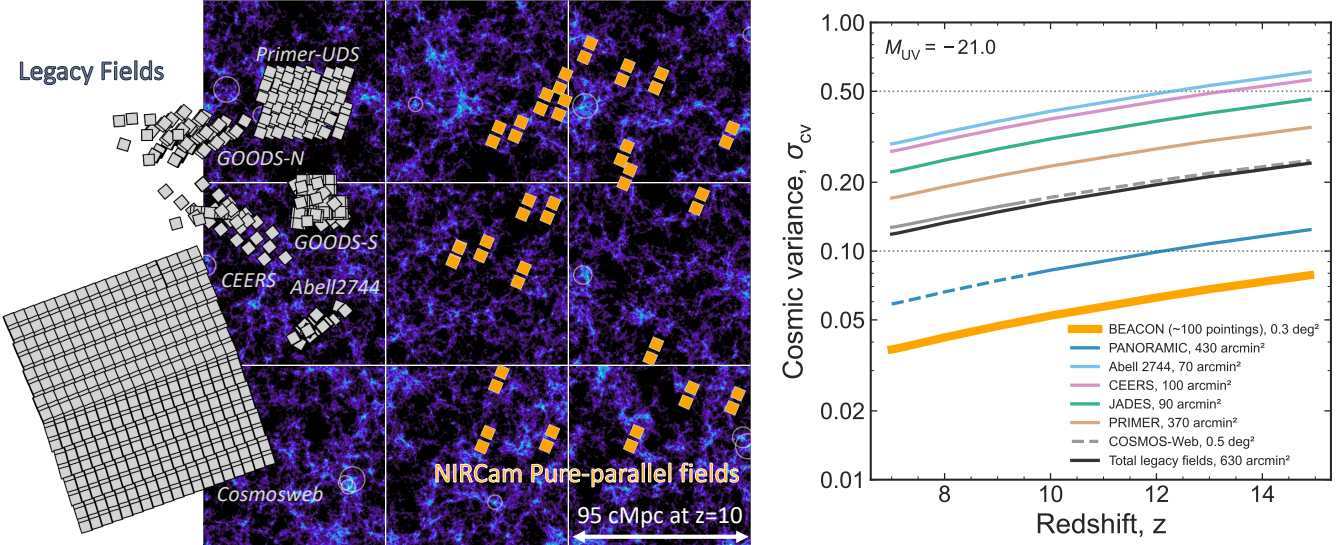


Figure 1. (Left): Schematics of NIRCam pure-parallel imaging. Each pair of squares (orange) indicates the size of NIRCam imaging fields, overlaid on dark matter distribution at $z = 10$ from the THESAN simulation (Kannan et al. 2022, each of the nine panel has a size of ~ 95 cMpc), where halos hosting massive galaxies ($> 10^8 M_\odot$) are encircled. For comparison, Cycle 1 and 2 surveys in legacy fields are shown (gray). (Right): Cosmic variance, σ_{cv} , in the UV luminosity function at $M_{UV} = -21$, as a function of redshift for several JWST imaging programs (colored lines), compared to the expected cosmic variance in BEACON (thick orange line), and the total cosmic variance in legacy fields observed with at least 8 NIRCam filters (Abell 2744, JADES, CEERS, PRIMER), all estimated using the cosmic variance calculator by Trapp & Furlanetto (2020) (see Section 2). Dashed lines indicate where contamination is expected to be high in surveys with fewer NIRCam filters.

ings. This enables a wealth of science investigations with minimal cosmic variance. We briefly describe our key science drivers.

2.1. Unbiased view of galaxies in the first billion years

Early JWST observations discovered an unprecedented abundance of intrinsically luminous $z \gtrsim 10$ galaxy candidates (e.g., Castellano et al. 2022; Naidu et al. 2022; Donnan et al. 2022; Harikane et al. 2023a; Bouwens et al. 2022; Casey et al. 2023). Those luminous galaxies were not expected by theoretical models (e.g., Dayal et al. 2014; Mason et al. 2015; Mashian et al. 2016; Tacchella et al. 2018; Behroozi et al. 2018; Yung et al. 2018; Wilkins et al. 2022), implying that some key physics is missing in the model of first galaxy formation. However, these detections have come from just ~ 600 sq. arcmin of public imaging in legacy fields, and are subject to significant cosmic variance. In Fig. 1, we show the fractional cosmic variance as a function of redshift in JWST Cycle 1-2 programs, compared to the predicted cosmic variance in BEACON observations. We estimate the cosmic variance in the UV LF ($\sigma_{cv}^2(\phi) = [\langle\phi^2\rangle - \langle\phi\rangle^2]/\langle\phi\rangle^2$) at $M_{UV} = -21$, i.e. comparable to the UV magnitude of the brightest $z > 12$ galaxies confirmed by JWST: GHZ2/GLASS-z12 (Castellano et al. 2022; Naidu et al. 2022) and JADES-GS-z14-0 (Carniani et al. 2024), using the calculator by Trapp & Furlanetto (2020). We calculate the cosmic variance

in multiple fields by summing the variance in quadrature following Trapp et al. (2022). Robustly measuring the bright end of the UV luminosity function (LF) and its evolution at $z > 7$ requires *large* samples of $z > 7$ sources over a wide luminosity range and sufficient areas, to maximize statistical robustness against cosmic variance. Crucially, Fig. 1 shows how independent-sightline surveys like BEACON and PANORAMIC (Williams et al. 2024) efficiently reduce cosmic variance compared to contiguous fields. The Trapp & Furlanetto (2020) model predicts that BEACON will reach $\sim 5\%$ cosmic variance in the bright-end of the UV LF at $z \sim 12$, compared to $\sim 20\%$ cosmic variance in both a comparable contiguous area with COSMOS-Web, which has a smaller filter set (4 NIRCam filters), and to the combination of deep JWST surveys in legacy fields (Abell 2744, CEERS, JADES, and PRIMER).

In Fig. 2, we show the expected number of galaxies that BEACON will find, assuming that the survey will reach 80% completeness down to 10σ limiting magnitudes. For the allocated 600 hrs (see also Sec. 3), we expect to find 500–1000 galaxies at $z \geq 7.3$ and 25–125 galaxies in the redshift range $9.7 \leq z \leq 13$, depending on the model used. The most interesting redshift range is $z \geq 13$, where the predicted numbers from different models deviate the most. For example, a model assuming redshift-independent star-formation efficiency even with no dust obscuration (Mason et al. 2015, 2023),

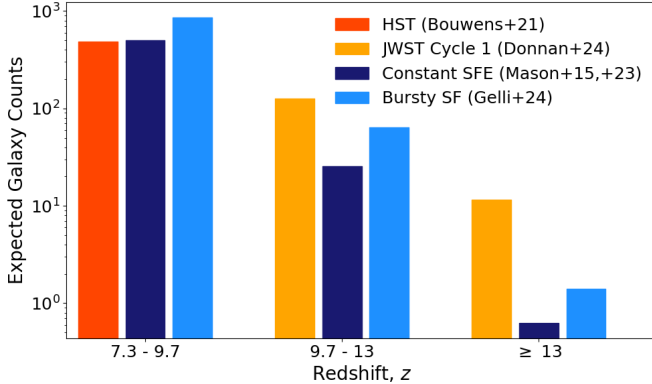


Figure 2. Expected numbers of sources in BEACON, shown for two theoretical models: constant star-formation efficiency (dark blue, Mason et al. 2015, 2023) and bursty star-formation (light blue, Gelli et al. 2024), and for two data-driven LFs: one determined from HST (red, Bouwens et al. 2021) and one from JWST Cycle 1 (orange, Donnan et al. 2024). All numbers are estimated assuming a flat 80% completeness down to the 10σ limiting magnitude. At $z \geq 13$ models predict hugely different number counts, thus BEACON will distinguish between scenarios.

predicts just one galaxy, whereas the LF based on early Cycle 1 fields (Donnan et al. 2024) predicts 12 galaxies and a bursty star formation model (Gelli et al. 2024) does a few. By the completion of our survey, we will have an improved census of galaxies in the first billion years.

2.2. Cosmic Noon — Build-up of stellar mass and structures

Galaxies at $z \sim 2$ appear significantly different from those in the local Universe — with clumpy and disturbed features from star formation (e.g., Elmegreen & Elmegreen 2005; Förster Schreiber et al. 2009; Genzel et al. 2011; Guo et al. 2015), or compact morphology for post-starburst and passively evolving galaxies (e.g., Daddi et al. 2005; Damjanov et al. 2009; Barro et al. 2017; Setton et al. 2022). The discovery of already quenched populations at $z > 3$ (e.g., Glazebrook et al. 2017; Schreiber et al. 2018; Tanaka et al. 2019; Valentino et al. 2020), some of which are clustered (Ito et al. 2023; Tanaka et al. 2024), suggests a very early and rapid build-up of stellar mass. Early JWST NIRCam studies identified several massive galaxies at $z \sim 4\text{--}7$ (Carnall et al. 2022, 2023; Glazebrook et al. 2023; Weibel et al. 2024). The prevalence of many evolved galaxies in such early epoch would invoke a critical, but intriguing, need of updates to the current galaxy evolution and quenching models (e.g., Boylan-Kolchin 2022; Lovell et al. 2023). Further identification requires a larger vol-

ume to build a complete picture of massive galaxy build-up.

BEACON will enable the search for massive galaxies at $2 < z < 7$, over a total volume of $\sim 10^7 \text{ Mpc}^3$. Based on our magnitude limits and the mass functions from Davidzon et al. (2017); Weaver et al. (2022), we expect that $\sim 10^5$ galaxies of $M_* > 10^9 M_\odot$ will be identified, including several $\log M_*/M_\odot > 3 \times 10^{10} M_\odot$ galaxies at $z > 5$. The star-formation activity of these galaxies will be characterized by, e.g., the rest-frame UVJ diagram (Williams et al. 2009; Valentino et al. 2023). The wavelength coverage from contiguous filters out to $\sim 5 \mu\text{m}$ will secure galaxy samples of currently missed quiescent and dust-enshrouded optical-dark galaxy populations (Wang et al. 2024; Barrufet et al. 2024), allowing for a comprehensive study of their properties, including their dependence on galaxy overdensity (Morishita et al. 2024a; Champagne et al. 2024). Furthermore, HST pure-parallels demonstrated statistics measured in many uncorrelated fields and provided novel measurements of galaxy/dark matter halo bias (Cameron et al. 2019). The superb photometric quality will enable searches for candidate over-densities of galaxies (e.g., Newman et al. 2014).

2.3. Nearby Universe — Dwarfs and galaxies

Early Release Science (ERS) and Cycle 1 programs clearly showed that a few hours of exposure time with JWST are comparable to the deepest fields observed by HST. BEACON will provide a unique and extensive dataset for legacy science, including enabling follow-up spectroscopy of exciting targets in future JWST cycles. Some legacy science highlights are:

(1) Study of brown dwarfs in the Milky Way, to probe its structure from random sightline observations (Ryan et al. 2011; Holwerda et al. 2014, 2018). The wavelength coverage at $>1.6 \mu\text{m}$ is critical to characterize (sub-)dwarf populations (Schneider et al. 2020; Nonino et al. 2022; Burgasser et al. 2024; Hainline et al. 2024).

(2) Dust properties of galaxies at $z \sim 0$: Stellar continuum and dust emission coexist in the rest frame $1\text{--}5 \mu\text{m}$. NIRCam filters will enable starburst/AGN diagnostics with F200W–F444W color (e.g., Vulcani et al. 2023) and $3.3 \mu\text{m}$ PAH features measured with F356W flux excess (e.g., Inami et al. 2018) for those with accurate redshift measurements.

3. SURVEY DESIGN

3.1. Pure-parallel Observations with JWST

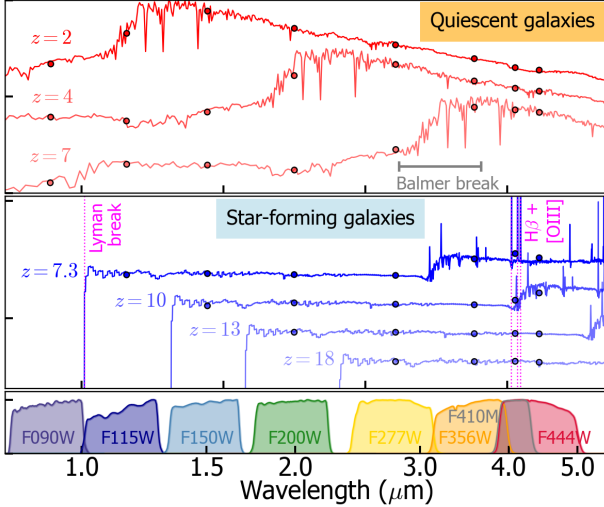


Figure 3. Template SEDs of galaxies at various redshifts, along with the transmission curves of our default filter set.

JWST offers a pure-parallel observing mode², in which one instrument is used while another serves as the primary. This is similar to the pure parallel mode operated by HST (Atek et al. 2011; Trenti et al. 2011; Yan et al. 2011). With JWST, pure-parallel observations can utilize a variety of instruments (i.e. NIRCam, NIRISS and MIRI as of Cycle 2). The pure-parallel use of NIRCam is analogous to the HST’s use of WFC3-IR, as seen in the BoRG survey (Trenti et al. 2011). However, there are significant differences with NIRCam’s pure-parallel imaging: 1) extended red wavelength coverage ($5\text{ }\mu\text{m}$ vs. $1.7\text{ }\mu\text{m}$), 2) a larger effective field-of-view (FoV) per image (9.7 arcmin^2 vs. 4.6 arcmin^2), and 3) dichroic imaging capability, allowing simultaneous short- and long-wavelength observations. The combination of the second and third points makes JWST’s NIRCam pure-parallel mode approximately four times more efficient than HST’s, even before considering the significant sensitivity differences (i.e. $m_H = 28.4\text{ mag}$ vs 26.6 mag at 10σ , 1 hr exposure). Additionally, JWST’s primary observing modes are typically equipped with dithering, which benefits parallel imaging by reducing potential contamination from detector artifacts and cosmic rays, whereas this has not been often the case for HST’s pure-parallel observations.

JWST’s pure-parallel mode, however, introduces high complexity, resulting in stringent requirements for scheduling and filter configurations. JWST does not allow mechanical movement during the primary dither, resulting in less flexibility when distributing exposure time

² <https://jwst-docs.stsci.edu/jppom/parallel-observations>

across multiple filters in a given pointing. Especially, JWST can offer a very long exposure per visit, whereas HST is limited to a maximum exposure $\sim 2800\text{ sec}$ due to the interruption from its orbit occultation. This in general helps the primary observations reduce the overhead, but it also means *fewer opportunities* for the parallel to reconfigure optical elements. Additionally, the complexity of the spectroscopic observing modes necessitates careful consideration of data rates, which in some cases results in less optimized for artifact rejections.

Among the allocated opportunities, we prioritized those that offer four or more “group slots” (corresponding to the number of short-/long-filter pairs) within the same field. As pure-parallel availability is determined by the setup of primary programs on the schedule, not all the allocated opportunities have at least four slots. Thus, we also utilize observations with fewer slots when they either (i) provide sufficient depth ($\gtrsim 1000\text{ sec}$) or (ii) include existing NIRCam data covering most of the FoV from previous observations, which can be combined with the new data. We discuss the selection of filters in more detail in Sec. 3.3.

3.2. Exposure Configuration

Each exposure is set to optimize the signal-to-noise ratio (SNR) and meet the data volume limitation. The total data volume is significantly affected by the configuration of each primary observation. As such, a careful consideration for each visit on the Astronomer’s Proposal Tool (APT) is required. Our default is to use the SHALLOW4 readout mode, which allows a reasonable exposure and SNR without suffering from saturation. When data volume is severely limited, we use a longer readout mode, i.e., DEEP8 or DEEP2, which are more subject to saturation for bright sources.

3.3. Filter Configuration

Taking advantage of NIRCam dichroic, our default filter configuration consists of 8 filters ($0.8 < \lambda/\mu\text{m} < 5.0$), pairing the four long-wavelength filters (F277W, F356W, F410M, F444W) with four short-wavelength ones (F090W, F115W, F150W, F200W; Fig. 3). This means that we require a minimum of four group slots in the primary program, where each group slot consists of an entire dither sequence. However, due to the limited availability of parallel slots, our program utilizes opportunities of less than 4 group slots (see below).

Those 8 NIRCam filters securely capture the Lyman break of galaxies at $z > 7$ and the Balmer break for galaxies at $2 < z < 7$. The almost uninterrupted, non-overlapping filter choice at $0.8\text{--}5\text{ }\mu\text{m}$ allows us a complete sampling of galaxies at these redshift ranges. In

addition to the Lyman break, the Balmer break sampled by F277W/F356W/F410M/F444W is critical to characterize stellar populations of galaxies at $z \lesssim 10.5$ (e.g., Witten et al. 2024; Katz et al. 2024), as well as to capture extreme line emission from H β +[O III] at $7 < z < 9$ by measuring flux excess in F410M/F444W (e.g., Endsley et al. 2022; Llerena et al. 2024). When five or more group slots are available, we include other medium-band filters (F140M, F182M, F210M, F430M, F460M) which increase the redshift reliability and expand the redshift range of strong-line emitter searches.

For parallel opportunities where only three group slots are available, we configure those with F090W, F115W, F150W, F277W, F356W, and F444W. This strategy keeps a redshift range similar to that for the full filter case. We utilize opportunities with fewer filters only when there are available data in the overlapping area; for those, we select unused filters to increase wavelength sampling.

We note that several visits so far were skipped in our executed observations, due to scheduling issues (unexpected changes in the primary observations) or data transfer limits during the visits. Consequently, those affected fields may have shorter total exposures than planned, or only partial filter coverage, or in some cases no observations.

4. DATA ANALYSIS OVERVIEW

4.1. Imaging Data Reduction

In this study, we reduce and analyze data taken in the first 19 fields. The sky distributions of the fields are shown in Fig. 4. We follow an approach similar to that presented by Morishita & Stiavelli (2023) for the reduction of images. Briefly, our pipeline retrieves the raw-level images from the Mikulski Archive for Space Telescopes (MAST) archive when they become available after each observation, and then reduces them with the official JWST pipeline. Our pipeline adds several custom steps including $1/f$ -noise subtraction using `bbpn`³, snowball masking using `Grizli` (Brammer et al. 2022), and additional cosmic-ray masking using `lacosmic` (van Dokkum 2001; Bradley 2023). The final drizzled images, with the pixel scale set to 0. $''$ 0315 / pixel, are aligned to the IR-detection image (F277W+F356W+F444W as the default choice).

To homogenize the PSF of the NIRCam images with that of F444W, we generate convolution kernels using PSFs generated with `webbpsf`⁴. We provide those PSFs

to `pypher` (Boucaud et al. 2016) and generate convolution kernels for each filter. The quality of convolved PSFs is within $\ll 1\%$ agreement in the encircled flux at radius $r = 0. $''$ 16$ i.e. the size used for our photometric flux measurements.

4.2. Photometry

We identify sources in the detection image using `SExtractor` (Bertin & Arnouts 1996). We measure source fluxes on point spread function (PSF)-matched mosaic images with a fixed aperture of radius 0. $''$ 16. We set the configuration parameters of `SExtractor` as follows: DETECT_MINAREA 0.0081 arcsec 2 , DETECT_THRESH 1.0, DEBLEND_NTHRESH 64, DEBLEND_MINCONT 0.0001, BACK_SIZE 128, and BACK_FILSIZE 5.

The aperture-based fluxes measured for each source are then scaled by a single factor, defined as $f_{\text{auto}, \text{F444W}} / f_{\text{aper}, \text{F444W}}$, to the total flux, where f_{auto} is the flux measured within elliptical Kron apertures with the 2.5 scaling factor. With this approach, colors remain as those measured in the aperture, whereas the fluxes used in the following analyses (for the derivation of stellar mass and star formation rate) are scaled up to the total quantities.

Once the fluxes are measured and scaled, Galactic dust reddening is corrected using the attenuation value retrieved for the coordinates of each field from NED (Schlegel et al. 1998; Schlafly & Finkbeiner 2011). We adopt the canonical Milky Way dust law for the reddening curve (Cardelli et al. 1989).

The average limiting magnitudes of the images are measured in regions where no source is detected among the effective area (i.e. sky area), using apertures of 0. $''$ 16 radius, and reported in Table 1. The average limiting magnitude of the DR1 fields and the total area are shown in Fig. 5, together with those of the aforementioned JWST surveys and several HST surveys (Koekemoer et al. 2011; Grogin et al. 2011; Ellis et al. 2013; Illingworth et al. 2013; Bouwens et al. 2019).

4.3. Photometric Redshift

For each field, we produce a photometric catalog by running `eazy` (Brammer et al. 2008). Our default setup is similar to what was presented in Morishita et al. (2023), using a template library provided by Hainline et al. (2023). This template library supplements `eazy`'s default library (v1.3) by adding young, line-emitting galaxy templates generated with `fsps` (Conroy et al. 2009). The increased variety of fitting templates thus

³ <https://github.com/mtakahiro/bbpn>

⁴ <https://github.com/spacetelescope/webbpsf>

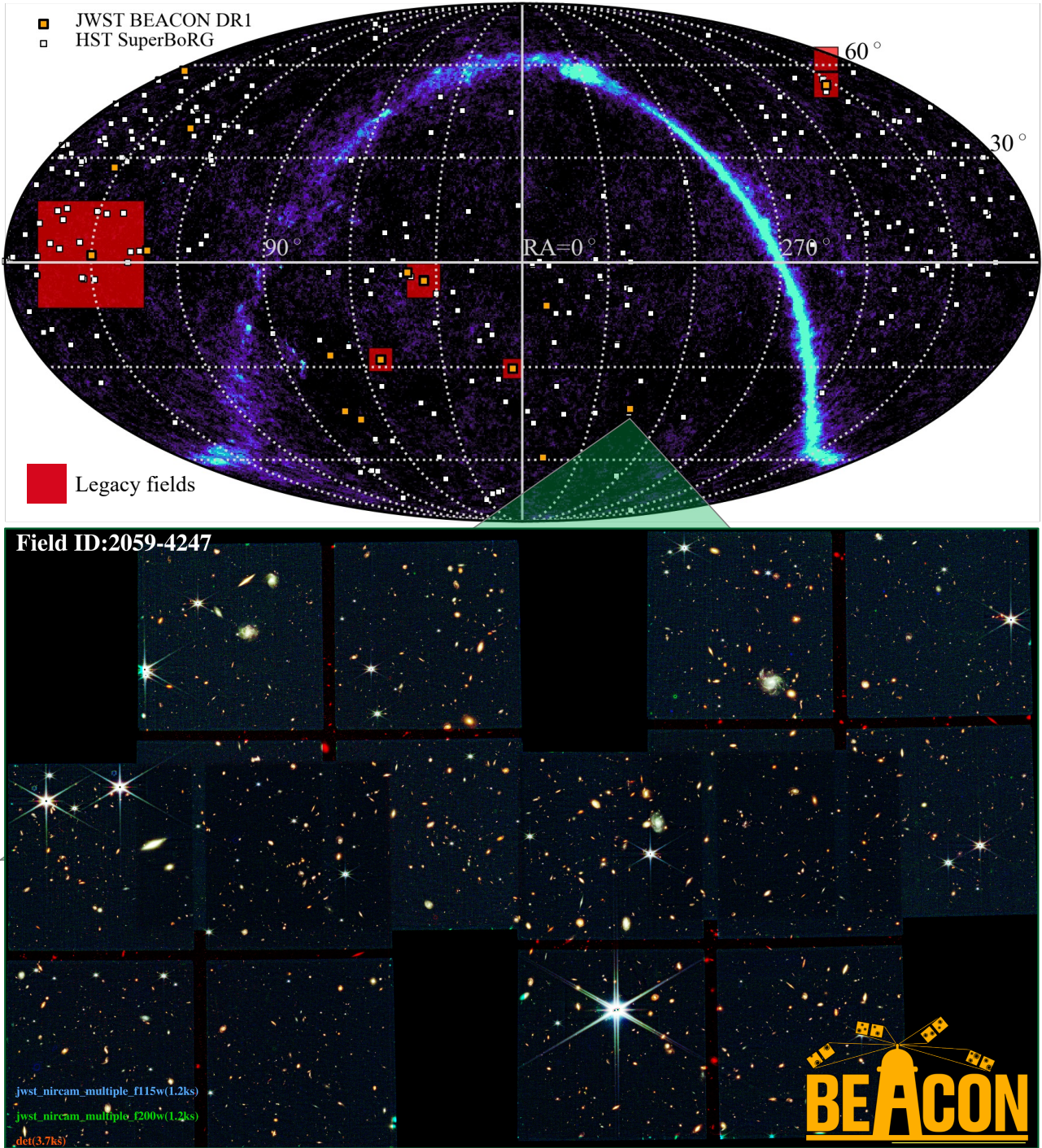


Figure 4. (Top): Sky distributions of the 19 BEACON DR1 fields (orange squares), overlaid on a temperature map from the WMAP 7-yr data (Jarosik et al. 2011). Also shown are legacy fields of JWST (COSMOS-Web, PRIMER-UDS, CEERS-EGS, JADES-GOODS-South, JADES-GOODS-North, and Abell2744; red squares) and the HST's pure-parallel imaging fields from HST SuperBoRG (white squares; $N = 316$). The symbol sizes are not the actual sky size, but are roughly scaled to the corresponding survey area. (Bottom): RGB-color composite image of one of the DR1 fields.

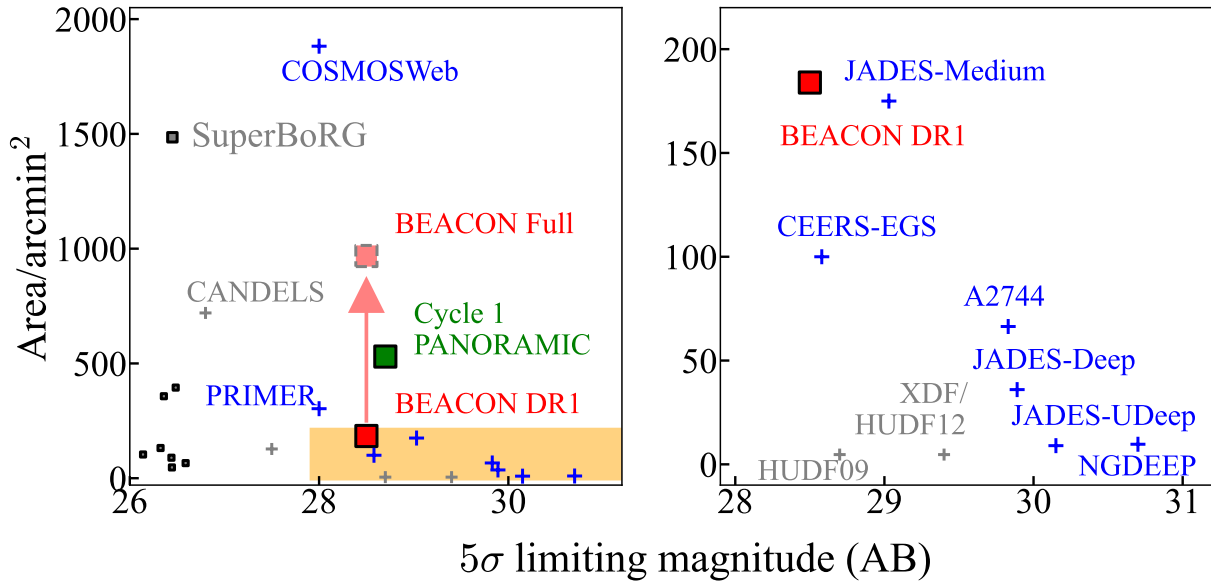


Figure 5. Limiting magnitudes and survey areas of various JWST programs (symbols in color). Square and cross symbols represent pure-parallel and for legacy surveys, respectively. Several HST programs are also shown in gray (see Morishita 2021 for the full description). The region hatched in orange is shown in zoom in the right panel.

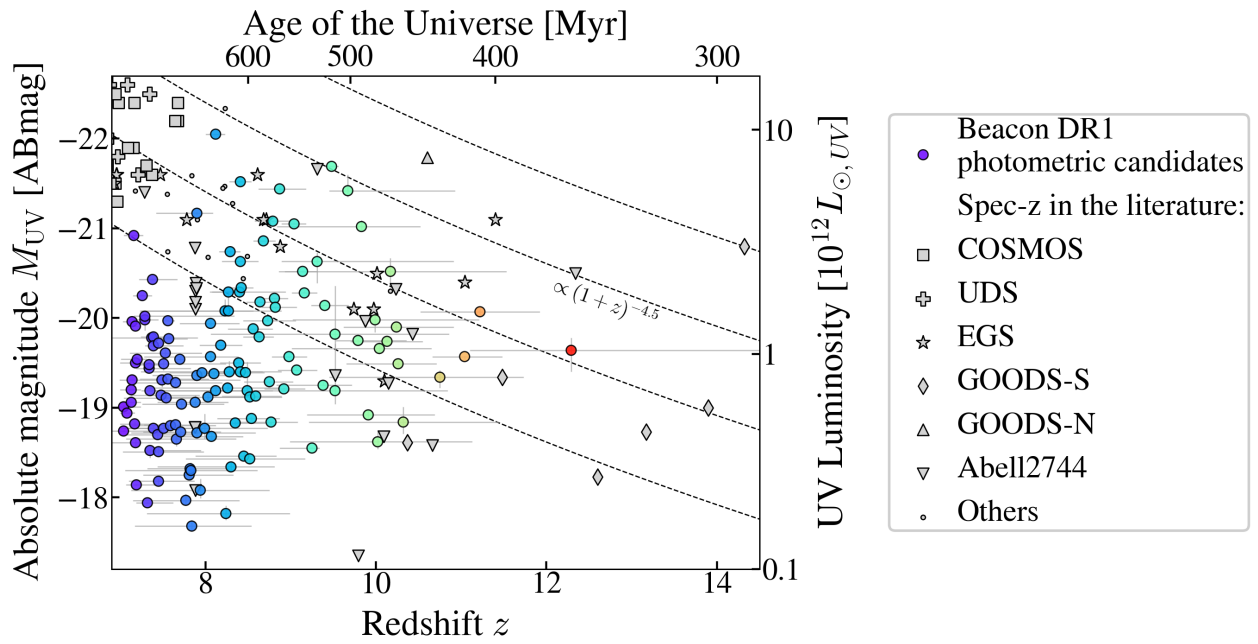


Figure 6. Redshift- M_{UV} distributions of final photometric candidates selected from the 19 DR1 fields (circles, colored by redshift). Semi-empirical luminosity evolution curves, $\propto (1+z)^{-4.5}$, of halos of a given comoving abundance are shown (dashed lines). Spectroscopically confirmed sources in the literature are shown (gray symbols; Curtis-Lake et al. 2023; Harikane et al. 2023b; Arrabal Haro et al. 2023; Morishita et al. 2023; Castellano et al. 2024; Roberts-Borsani et al. 2024b; Napolitano et al. 2024; Carniani et al. 2024).

Table 1.

FLDID	R.A.	Decl.	F090W		F115W		F150W		F200W		F277W		F356W		F410M		F444W	
			deg.	deg.	t_{exp}	$m_{5\sigma}$												
0014-3025	3.59520	-30.41974	10.0	28.9	10.0	28.8	—	—	10.0	29.1	10.0	29.1	10.0	29.3	—	—	10.0	29.0
0217-0509	34.21885	-5.13408	18.9	29.3	13.1	29.0	13.1	29.2	—	—	13.1	29.1	13.1	29.2	—	—	18.9	28.8
0217-0508	34.29253	-5.12272	18.9	29.4	13.1	29.0	13.1	29.2	—	—	13.1	29.2	13.1	29.2	—	—	18.9	28.9
0217-0504	34.30829	-5.07792	18.9	29.2	13.1	29.0	13.1	29.2	—	—	13.1	29.5	13.1	29.6	—	—	18.9	29.3
0240-0253	40.09595	-2.87019	1.0	26.9	1.0	26.9	1.0	27.2	—	—	1.0	28.0	1.0	28.1	—	—	1.0	27.5
0332-2749	53.03300	-27.81392	16.1	29.4	16.1	29.4	1.2	28.0	16.1	29.7	16.1	29.4	1.2	28.5	16.1	29.1	16.1	29.3
0332-2745	53.03766	-27.75151	7.5	28.9	7.5	29.0	7.5	29.1	12.5	29.3	7.5	29.6	7.5	29.5	—	—	20.0	29.2
0442-4613	70.42773	-46.21713	0.7	26.6	0.5	26.1	0.5	26.4	—	—	0.5	27.5	0.5	27.5	—	—	0.7	27.7
0447-2637	71.67559	-26.60116	1.2	27.6	1.2	27.4	1.2	27.9	1.2	28.1	1.2	28.6	1.2	28.5	1.2	27.9	1.2	28.2
0502-4338	75.45100	-43.63230	—	—	1.0	27.5	1.0	27.8	1.0	28.0	1.0	28.5	1.0	28.5	—	—	1.0	28.2
0843+0324	130.65348	3.41877	—	—	0.8	27.6	0.8	27.8	0.8	27.9	0.8	28.3	0.8	28.3	—	—	0.8	27.8
0860+3857	134.98519	38.96236	2.5	27.9	1.6	27.5	1.6	27.7	—	—	1.6	28.5	1.6	28.5	—	—	2.5	28.2
0959+0200	149.84149	2.01664	3.3	28.3	3.3	28.3	3.3	28.5	3.3	28.6	3.3	28.9	3.3	28.9	3.3	28.2	3.3	28.5
1010+2701	152.44541	27.03744	4.2	28.1	4.2	28.1	4.2	28.4	—	—	4.2	28.7	4.2	28.7	—	—	4.2	28.3
1138+5748	174.41601	57.80085	1.4	27.4	1.4	27.3	1.4	27.6	—	—	1.4	28.5	1.4	28.4	—	—	1.4	28.1
1420+5252	215.07468	52.86999	3.4	28.0	3.4	28.1	3.4	28.3	3.4	28.5	3.4	28.9	3.4	28.9	3.4	28.2	3.4	28.6
2059-4247	314.63703	-42.78990	—	—	1.2	27.0	1.2	27.3	1.2	27.4	1.2	28.0	1.2	28.1	—	—	1.2	27.6
2316-5910	349.11637	-59.15965	—	—	1.8	27.0	1.8	27.3	1.8	27.5	1.8	28.1	1.8	28.2	—	—	1.8	27.8
2325-1216	351.35492	-12.26333	—	—	1.0	26.5	1.0	26.8	1.0	26.8	1.0	27.7	1.0	27.8	—	—	1.0	27.6

NOTE— 5- σ limiting magnitudes for point sources are shown. Exposure times are shown in the units of 1000 seconds.

enables a more comprehensive redshift estimate for target young galaxies. The redshift range of fitting is set to $0 < z < 30$, with a step size of $0.01(1+z)$. We adopt a default magnitude prior provided by `eazy`, using one of the three NIRCam red channel broad filters (F277W, F356W, F444W) based on their availability in each field.

We utilize the output likelihood function derived by `eazy` to estimate a statistical redshift range for each source. We adopt the median redshift calculated using the full $p(z)$ distribution as the best-fit redshift, and estimate 1σ uncertainties by taking the differences from the 16th and 84th percentile redshifts. The redshift measurements and the probability distributions are used in our high- z galaxy selection (Sec. 5.2). Absolute UV magnitudes (M_{UV}) are calculated using the best-fit template at the corresponding redshifts.

4.4. Photometric Selection of High-Redshift Galaxies

We identify candidate galaxies at $z > 7$ via the Lyman-break dropout method (Steidel et al. 1998). Following a similar approach presented in Morishita & Stiavelli (2023); Morishita et al. (2024b), we first apply the following color selection:

F090W-dropouts ($7.3 \lesssim z \lesssim 9.7$)

$$S/N_{150} > 4$$

$$S/N_{090} < 2$$

$$z_{\text{set}} = 6$$

F115W-dropouts ($9.7 \lesssim z \lesssim 13$)

$$S/N_{200} > 4$$

$$S/N_{115,090} < 2$$

$$z_{\text{set}} = 8$$

F150W-dropouts ($13 \lesssim z \lesssim 18$)

$$S/N_{277} > 4$$

$$S/N_{150,115,090} < 2$$

$$z_{\text{set}} = 10$$

where available filters that are bluer than the rest-frame wavelength of $< 1216 \text{ \AA}$ are used for 2σ non-detection. Furthermore, to secure non-detection, we repeat the non-detection step with a smaller aperture, $r = 0.^{\prime\prime}08$ (~ 2.5 pixel). Note that a photometric selection is not attempted for redshift windows where no dropout filter is available. z_{set} is a redshift limit used to calculate total low- z probabilities (see below).

After securing non-detection in blue filters, we apply a photometric redshift selection. Following Morishita et al. (2018), in each dropout selection we exclude sources that do not satisfy $p(z > z_{\text{set}}) > 0.8$, i.e. total redshift probability at $z > z_{\text{set}}$ is less than 80%,

where z_{set} is defined above separately for each selection redshift window. The combination of the detection/non-detection requirement and the phot- z analysis provides us with sources whose phot- z solution is consistent with the dedicated redshift range of each dropout selection.

5. INITIAL RESULTS

5.1. Overview of the Observed Fields

In this overview paper, we focus on the first 19 fields taken (hereafter Data Release 1, or DR1, fields). Results from the full fields will be presented upon completion of the program in forthcoming papers. In Tab. 1, we summarize the DR1 fields. Limiting magnitudes, calculated for a fixed aperture size, are listed.

Some fields overlap with previous extragalactic JWST fields, including Abell 2744 (Treu et al. 2022; Labbe et al. 2023), COSMOS (Casey et al. 2022), AEGIS (Bagley et al. 2023), UDS (Donnan et al. 2024), and GOODS-South/North (Hainline et al. 2023). As mentioned previously, in those overlapping fields we supplement the filters that were not previously used (especially F090W; and when possible use medium filters such as F140M/F182M/F210M/F430M/F480M), to enable searches of emission line galaxies at $7 < z < 9$ and improve photometric-redshift accuracy.

5.2. Identification of $z > 7$ galaxies

From the DR1 fields, we have identified 129 galaxy candidates at $z > 7$, consisting of 118 F090W-dropouts, 11 F115W-dropouts, and zero F150W-dropouts. In Fig. 6, we show the redshift- M_{UV} distribution of the selected sources. The faint end of the UV magnitude probed here is ~ -18 mag, consistent with the prediction by the exposure time calculator. We observe several luminous (< -21 mag) galaxies at $8 < z < 10$. As we see below (Sec. 5.3), the observed number of those luminous galaxies is overall consistent with pre-JWST studies (e.g., Bouwens et al. 2015; Stefanon et al. 2019), post-JWST (Leung et al. 2023; Willott et al. 2024), and also theoretical predictions (e.g., Mason et al. 2022).

On the other hand, at $z > 10$ we do not find many luminous galaxies that are comparable to GN-z11 (Oesch et al. 2018; Bunker et al. 2023; Tacchella et al. 2023), GHZ2 (Castellano et al. 2022; Naidu et al. 2022), and JADES-GS-z14-0 (Carniani et al. 2024). Also shown in Fig. 6 are spec- z confirmed sources in the literature. Interestingly, while the total area of the Beacon DR1 is comparable to those in the literature, we seem to be lacking luminous (< -20 mag) galaxies at $z > 10$, casting a doubt on our selection being too conservative. However, we confirmed that our color selection would successfully reproduce 12 of the 13 sources at $z_{\text{spec}} > 10$. The only

unsuccessful case (GS-z10-0; Curtis-Lake et al. 2023) is a faint galaxy ($m_{200} \sim 29$ mag) and thus our phot- z estimate has large error bars ($z_{\text{phot}} = 2.5^{+8.8}_{-2.2}$ at 1σ). Given the high success rate of our color selection, we suspect that the difference in $z > 10$ galaxy number densities may originate in cosmic variance. In fact, 6 and 3 of the $z_{\text{spec}} > 10$ sources are located in the GOODS-South field and one CEERS pointing, respectively. A further investigation of cosmic variance will be presented in our future work (Kreilgaard, in prep.).

5.2.1. Overview of Individual High- z Galaxy Candidates

The cutout images and SEDs of example $z \gtrsim 8$ candidates are shown in Fig. 7. At the redshift range of $z < 10$, we highlight two UV luminous galaxies. These examples showcase a variety of spectral features: ID336 is best fitted with an extreme emission line template, characterized by a blue rest-frame UV slope, and flux excess in the F444W band. ID2768 is located in the field beacon_1420+5252, where several medium bands are also taken (F140M, F182M, F410M, F430M, F480M). Red medium-band filters sample the wavelength around the Balmer break and thus effectively discriminate other possible solutions, e.g., line excess due to strong H β +[O III] emission lines, as seen in ID336.

We have identified 11 $z \gtrsim 10$ galaxies of moderate brightness, $-M_{\text{UV}} \sim 18.5\text{--}20.5$. Although the photometric flux errors are relatively large, leading to larger z uncertainties, all of these candidates are secured with a clear dropout in the F090W and F115W bands. At $z > 9$, H β +[O III] lines are redshifted to $> 5\,\mu\text{m}$ and thus a relatively flat slope is expected at $\sim 2\text{--}5\,\mu\text{m}$. In Fig. 7, we show two example sources from the redshift. ID13052 has a secondary solution at $z \sim 2.4$. The existing photometry, however, the low- z solution at $\sim 2\,\mu\text{m}$ discriminates. ID6608 is one of the highest-redshift candidates among our final sample. It has a relatively wide redshift probability distribution at $z > 10$, which is partially attributed to the fact that the spectrum is rather featureless for the observed wavelength range. However, the redshift probability at $z < 10$, with a secondary solution at $z \sim 3.6$, is low ($p(z < 10) = 0.004$), making it a likely high- z candidate.

Also noted is that most of the selected candidates have extended morphologies. While the multi-band NIRCam filters up to $\sim 5\,\mu\text{m}$ effectively eliminates the contamination of fore-ground low-mass stars (see Sec. 5.4), the morphological information (e.g., size, elongation, light concentration) of the color-selected source can further secure the final high- z sample (Zhang, in prep.).

5.3. Number Densities of UV-selected Galaxies at $z > 7$

Using the selected candidates, we aim to estimate the number density of galaxies at $z > 7$. An unusual aspect of our survey is that each field has different depths and filters. This results in completeness and selection functions that vary from field to field, requiring a careful effective volume estimate in each field.

For the effective volume estimate, we use an adaptation of the `GLACiAR2` completeness simulation code (Leethochawalit et al. 2022, 2023). Briefly, in each field, we inject 1200 galaxies into each magnitude-redshift bin. The bins run from $z = 6$ to 18 and from $M_{\text{UV}} = -18.5$ to -24 mag with an increment of 0.5 in both directions. The injected galaxies are assumed to have a Sérsic profile of $n = 1$ with the sizes that follow the M_{UV} -size relation as a function of redshift in Morishita et al. (2024b). The spectral shapes of the galaxies are randomly pulled from the JAGUAR (Williams et al. 2018) catalogs of the same redshift bin up to $z = 12$. Since there are not many spectra at $z > 12$ in the JAGUAR catalog, we combine all $z > 12$ JAGUAR spectra into one spectral pool. The images of the injected galaxies are convolved with the PSF from the F444W band and injected into the PSF-matched images. The detection, photometric extraction, and sample selection of the injected galaxies are done in the same manner as the real sources.

We then calculate the effective volume of each field as in Leethochawalit et al. (2023):

$$V_{\text{eff}}(M_{\text{recov}}) = \int \frac{dV}{dz} P(M_{\text{recov}}, z) dz. \quad (1)$$

$P(M_{\text{recov}}, z)$ is the number of simulated galaxies at redshift z that are recovered to have UV magnitude in the bin M_{recov} (regardless of their intrinsic UV magnitude), divided by the number of injected galaxies at redshift z with intrinsic UV magnitude equal to M_{recov} . For reference, at the brightest magnitude bins (i.e. $\sim 100\%$ completeness), the effective volumes for a single NIR-Cam pointing are approximately $2 \times 10^4 \text{ Mpc}^3$ for all redshift windows. Once effective volumes are calculated, we calculate the number density at each absolute UV magnitude bin by combining all fields.

The estimated galaxy number densities are shown in Fig. 8. Our estimates are overall consistent with studies in the literature at $7 < z < 13$ (Harikane et al. 2022; Donnan et al. 2022; Bouwens et al. 2022; Casey et al. 2023; Franco et al. 2024; Willott et al. 2024; Adams et al. 2024). Our estimates are also consistent with the theoretical prediction of Mason et al. (2023). The total effective volumes and the calculated number densities are listed in Tab. 2.

To assess our results in more detail, we fit the number density estimates with the Schechter (1976) function:

$$\phi(M_{\text{UV}}) = \frac{\ln 10}{2.5} \phi^* \times 10^{0.4(\alpha+1)(M_{\text{UV}} - M^*)} \times \exp[-10^{-0.4(M_{\text{UV}} - M^*)}] \quad (2)$$

using a Markov Chain Monte Carlo (MCMC) method (e.g., Morishita et al. 2018). The derived parameters for the $7.3 < z < 9.7$ number density are $\alpha = -2.07^{+0.23}_{-0.18}$, $\log \phi^* = -4.66^{+0.53}_{-0.44}$, and $M^* = -21.97^{+0.73}_{-0.66}$. For the $9.7 < z < 13$ range, we fix the slope to $\alpha = -2$ and find $\log \phi^* = -4.57^{+2.10}_{-0.96}$ and $M^* = -21.01^{+1.61}_{-1.45}$.

We estimate that we will find ~ 650 galaxies at $7.3 < z < 9.7$ and ~ 100 at $9.7 < z < 13$ in the full BEACON dataset, by using our LF estimates and simply scaling the survey volume while assuming 80% completeness down to the 10σ limiting magnitude. Our LF predicts similar numbers of galaxies to those of the constant star formation efficiency model by Mason et al. (2023) as in Fig. 2.

Despite covering a considerably large total area ($\sim 180 \text{ arcmin}^2$), there are no $z > 13$ galaxy candidates selected in our final samples. We place upper limits for the number densities (Fig. 8). The upper limits derived are still consistent with previous studies in legacy fields (Harikane et al. 2022; Donnan et al. 2024; McLeod et al. 2024), except for Robertson et al. (2024) at the bright end ($M_{\text{UV}} \sim -21$) which contains the luminous $z = 14$ galaxy GS-z14-0. The absence of luminous $z > 13$ galaxies in our fields may suggest a significant impact from cosmic variance affecting the statistics in those legacy fields. As we see in Sec. 5.1, a large fraction of $z_{\text{spec}} > 10$ sources are located just in *two* fields. In addition, exceptionally luminous sources in the literature (GN-z11, GHZ2/GLASS-z12, GS-z14-0) are found in fields of relatively high cosmic variance ($\sigma_{\text{cv}} > 0.4$; Fig. 1). The complete data set of BEACON will reach a $5 \times$ larger volume ($\sim 1.5 \times 10^6 \text{ Mpc}^3$) and facilitate us to explore this further.

5.4. Ancillary Science

Our pure-parallel survey will provide a unique and extensive dataset for legacy science at lower redshifts. In particular, our filter coverage can secure key spectral features, such as the Balmer break of $z \sim 2$ galaxies (Fig. 3) and the $3.3 \mu\text{m}$ PAH emission line of $z \sim 0.3$ galaxies seen as a flux excess in F410M (e.g., Vulcani et al. 2023). In Fig. 9, we show two galaxy examples selected from the DR1 fields: a passively evolving galaxy at $z \sim 1.9$ and a dusty galaxy at $z \sim 4$. Also, foreground low-mass stars (brown dwarfs) are often found

as contaminants in high- z galaxy color selection, for its similar spectral features i.e. the color break at observed $\sim 1\,\mu\text{m}$ (Morishita et al. 2020; Ishikawa et al. 2022, also Greene et al. 2023 for spectroscopic confirmation of faint brown dwarf stars). The NIRCam data from BEACON securely discriminate those stars from galaxy populations by adding longer wavelength data points at $> 2\,\mu\text{m}$. The secure selection of faint stars enables us to study, e.g., their spatial distribution in the Milky Way halo (e.g., Ryan et al. 2011; Holwerda et al. 2014). In Fig. 9, we show one M-dwarf candidate, selected from spectral template fitting using the SPEX library (Rayner et al. 2003) and additional morphological analysis for point source selection.

Lastly, we expect some fraction of our fields to overlap with the existing survey fields where previous NIRCam fields are available. This is because long-exposure spectroscopic observations tend to target sources found within those popular legacy fields. In the DR1 fields, seven are found within the legacy fields (Fig. 4). Those overlapping fields are ideal for the detection of transient events and variability studies (e.g., Kokubo & Harikane 2024; Zhang et al. 2024).

6. SUMMARY

In this paper, we introduced BEACON, a new pure-parallel imaging survey scheduled in JWST Cycle 2. Using the first 19 fields, we established our data reduction processes and performed an initial high- z galaxy search. Through our careful color selection utilizing 6–8+ NIRCam filters, we identified 129 galaxy candidates at $7 < z < 13$. The galaxy number densities estimated in the fields are overall consistent with the previous estimates in the literature. Although our exploration reached a considerably large area ($\sim 180\,\text{arcmin}^2$), we found zero $z > 13$ galaxies. However, the upper limits of the $z > 13$ galaxy number density are consistent with previous studies in the literature. Further exploration utilizing the full BEACON dataset will confidently determine the contribution of cosmic variance to the number densities of bright $z > 13$ galaxies detected so far with JWST.

The BEACON dataset also allows for a range of lower- z science cases, such as the search for massive galaxies at cosmic noon and foreground low-mass stars. We plan to process all imaging data and publish the resulting products, including photometric flux redshift catalogs for each survey field. We will also make available the effective volume estimate from our completeness simulation. We will publish the data products of the DR1 fields on a dedicated website. Catalog data models are

Table 2. Number density of galaxies at $z > 8$

M_{UV} (mag)	Volume ^a ($10^3\,\text{Mpc}^3$)	N_{obj}	Number density ^b ($\log \text{Mpc}^{-3}\,\text{mag}^{-1}$)
F090W-dropout			
−23.0	366.9	0	< -5.30
−22.0	366.5	3	$-5.09^{+0.34}_{-0.29}$
−21.0	344.6	11	$-4.50^{+0.16}_{-0.11}$
−20.0	282.0	33	$-3.93^{+0.08}_{-0.07}$
−19.0	143.0	54	$-3.42^{+0.06}_{-0.06}$
−18.0	13.3	13	$-3.01^{+0.14}_{-0.11}$
−17.0	0.1	0	< -1.74
F115W-dropout			
−23.0	394.4	0	< -5.33
−22.0	365.1	0	< -5.30
−21.0	276.2	2	$-5.14^{+0.45}_{-0.36}$
−20.0	152.2	8	$-4.28^{+0.18}_{-0.17}$
−19.0	52.1	5	$-4.02^{+0.24}_{-0.22}$
−18.0	2.4	0	< -3.13
−17.0	0.1	0	< -1.64
F150W-dropout			
−23.0	355.7	0	< -5.29
−22.0	328.1	0	< -5.25
−21.0	249.3	0	< -5.14
−20.0	133.3	0	< -4.86
−19.0	33.9	0	< -4.27
−18.0	2.0	0	< -3.04
−17.0	0.1	0	< -1.89

Notes.

^a Effective volume calculated by the completeness simulation.

^b $1\,\sigma$ uncertainty calculated for small number statistics as in Gehrels (1986).

presented in Tab. 4. The full data release will be made when the program is complete.

ACKNOWLEDGEMENTS

We thank the program coordinators of our JWST program, Shelly Meyett and Blair Porterfield, and the instrument scientist, Anton Koekemoer, for their invaluable assistance in configuring our observations. In addition to being one of the largest JWST programs, the complexity of the pure-parallel mode introduced a series of unique challenges and issues, each of which benefited greatly from their expertise and perspectives. We also thank the Cycle 1 and 2 pure-parallel program teams

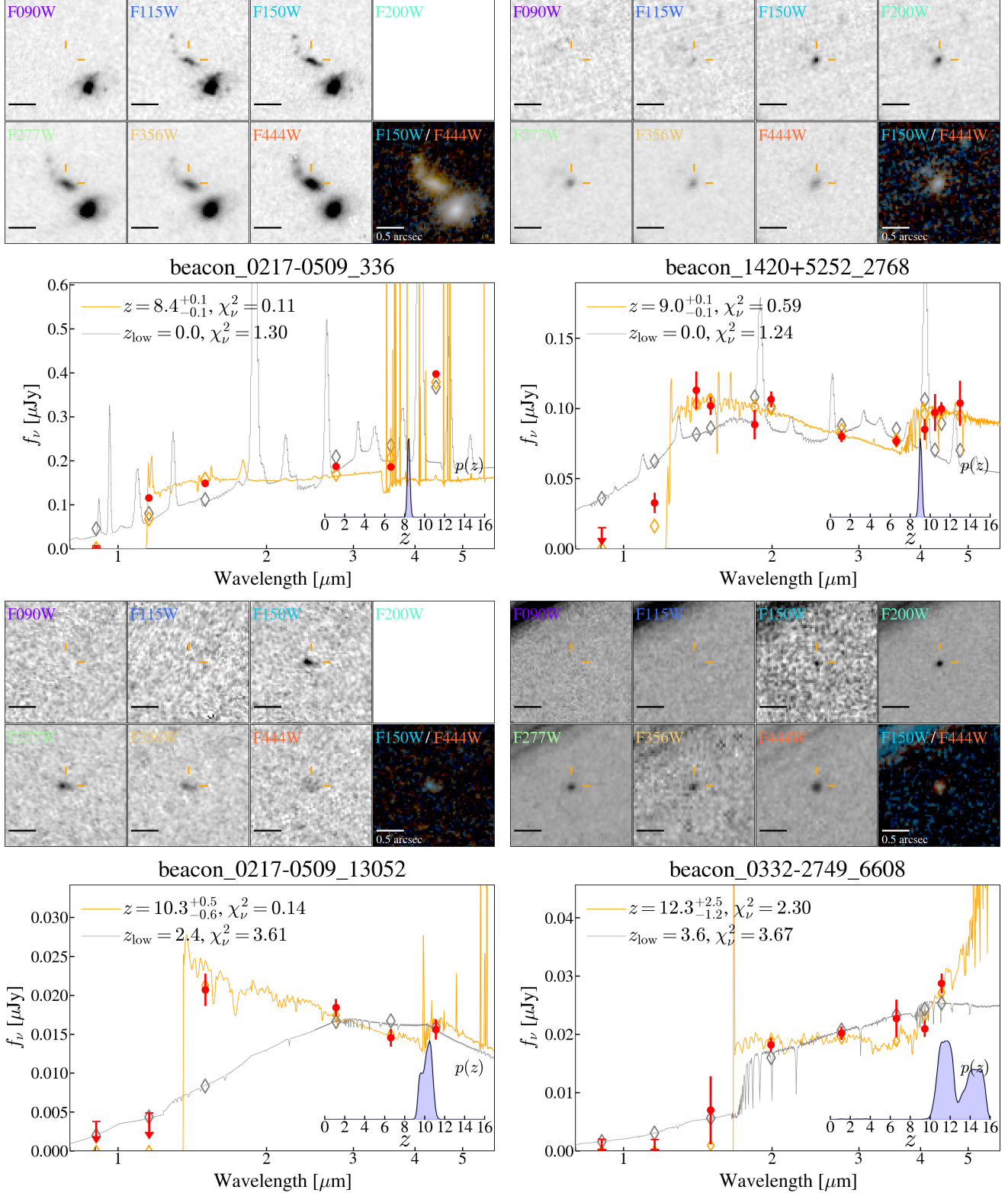


Figure 7. Postage stamps and SEDs of example high- z galaxy candidates. The best-fit flux models at high redshift (orange lines) and at the secondary low redshift (z_{low} , gray line) are shown. Photometric redshift probability distributions derived from EAzY are shown in the inset. The y-axis is set in a linear scale.

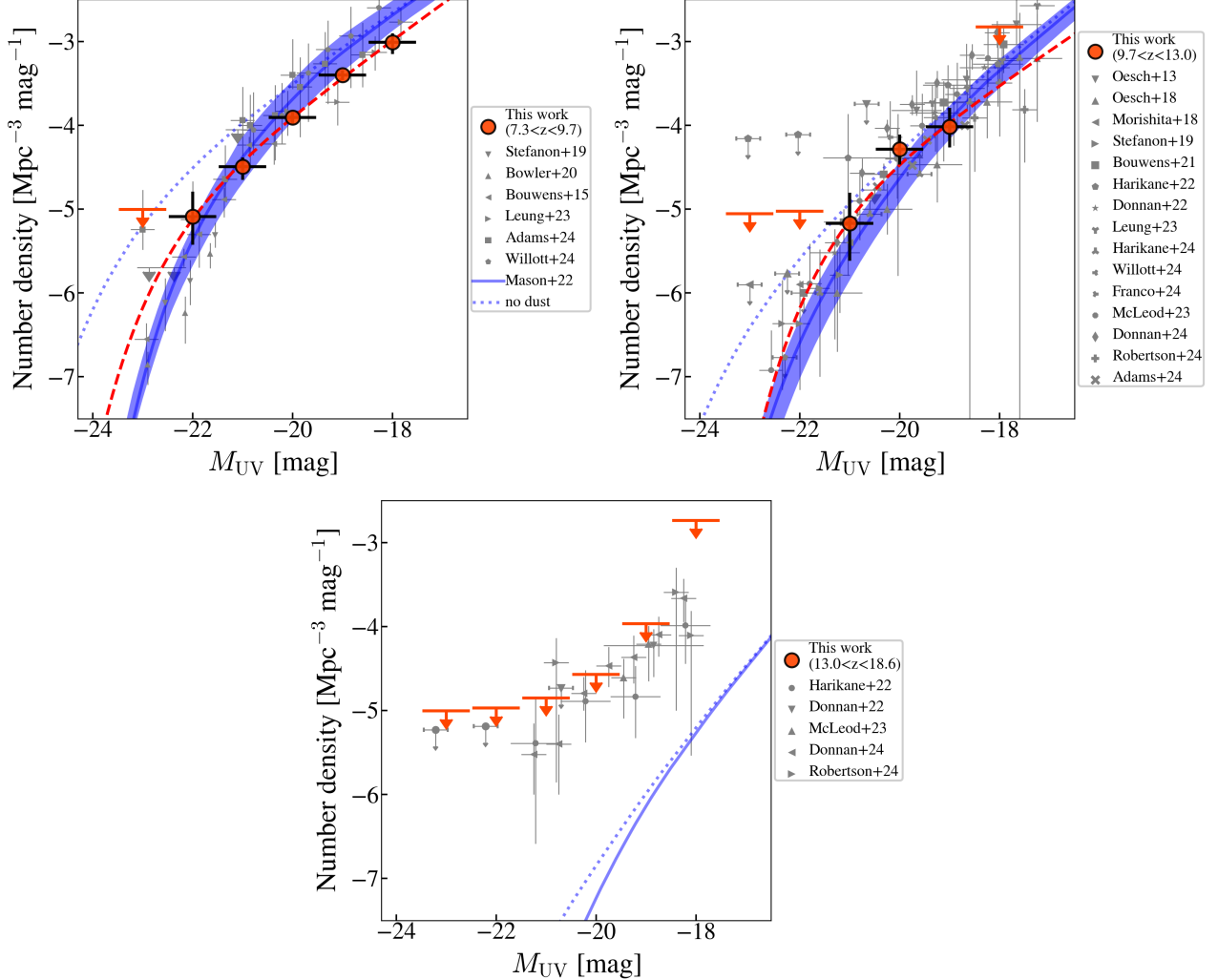


Figure 8. Number densities estimated for the Beacon DR1 sources (red circles and upper limits), at $z \sim 8.5$ (left top), $z \sim 11$ (right top), and $z \sim 15$ (bottom). For magnitude bins without any sources, we show $2-\sigma$ upper limits. The Schechter fit to our number density estimates is shown (red dashed lines). Number density estimates in the literature are shown (gray symbols; Oesch et al. 2013; Bouwens et al. 2015, 2021; Morishita et al. 2018; Stefanon et al. 2019; Donnan et al. 2022; Harikane et al. 2022, 2023a; McLeod et al. 2024; Leung et al. 2023; Willott et al. 2024; Rojas-Ruiz et al. 2024; Franco et al. 2024; Adams et al. 2024). The Mason et al. (2023) LFs (blue solid lines for the dust model, dashed lines for the no-dust model) of the corresponding redshift are shown. The redshift variation of the dust model is shown by a hatched region.

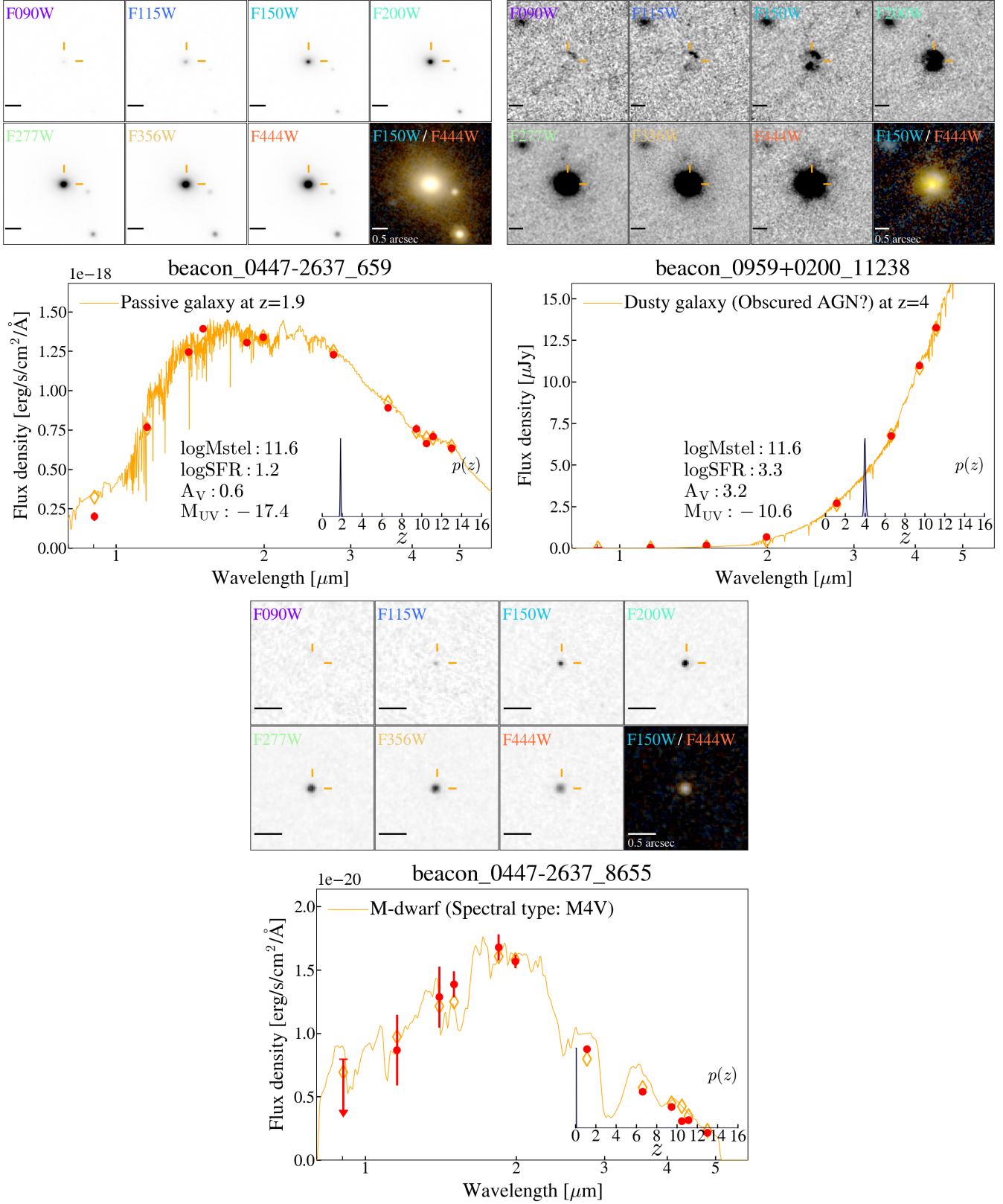


Figure 9. Examples of low- z sources from BEACON. The figure format is the same as in Fig. 7. *Left:* Massive ($\log M_*/M_\odot \sim 11.6$), passively evolving galaxy at $z \sim 1.9$. *Right:* Dusty galaxy at $z \sim 4$. The galaxy is characterized with a red spectral shape ($A_V \sim 3.2$). It has a compact point source (possibly obscured AGN) dominating at $> 2\mu\text{m}$, whereas extended structures are seen in bluer wavelengths. *Bottom:* faint ($m_{F200W} = 25.6$), M4V dwarf selected from point-source analysis and spectral template fitting. The best-fit spectral template (M4V) from the SPEX library (yellow line) is shown.

(PASSAGE, PANORAMIC, and PID 3383 (PI Glazebrook)) for their pioneering efforts, which laid the essential foundation and facilitated the operation of pure-parallel observations. We thank Xuejian Shen (MIT) and the THESAN team for sharing dark-matter density maps and related physical property catalogs from their simulations. TM and YZ thank George Helou for generously supporting our data analysis at IPAC. Support for program 3990 was provided by NASA through the Space Telescope Science Institute, which is operated by the Association of Universities for Research in Astronomy, Inc., under NASA contract NAS 5-03127. All of the data presented in this paper were obtained from the Mikulski Archive for Space Telescopes (MAST) at the Space Telescope Science Institute. The specific obser-

vations analyzed can be accessed via [10.17909/q8cd-2q22](https://doi.org/10.17909/q8cd-2q22). CAM, KCK and VG acknowledge support from the Carlsberg Foundation under grant CF22-1322. The Cosmic Dawn Center (DAWN) is funded by the Danish National Research Foundation under grant DNRF140. BV acknowledges support from the European Union – NextGenerationEU RFF M4C2 1.1 PRIN 2022 project 2022ZSL4BL INSIGHT. MB acknowledges support from the ERC Grant FIRSTLIGHT and Slovenian national research agency ARIS through grants N1-0238 and P1-0188.

Software: AstroML (Vanderplas et al. 2012), Astropy (Astropy Collaboration et al. 2013, 2018, 2022), bbpn (Morishita 2023), EAzY (Brammer et al. 2008), EMCEE (Foreman-Mackey et al. 2013), numpy (Harris et al. 2020).

Table 3. Selected high- z galaxy candidates.

ID	R.A.	Decl.	$m_{\text{F}150\text{W}}$	$m_{\text{F}444\text{W}}$	z	M_{UV}
beacon_0217-0509-1447	34.225235	-5.182756	28.1	27.5	$7.04^{+0.20}_{-0.18}$	$-19.01^{+0.01}_{-0.02}$
beacon_0217-0508-9736	34.293415	-5.115285	28.4	28.7	$7.04^{+0.37}_{-0.18}$	$-18.74^{+0.01}_{-0.01}$
beacon_1420+5252-7386	215.037430	52.877472	28.2	27.4	$7.08^{+0.09}_{-0.08}$	$-18.94^{+0.01}_{-0.01}$
beacon_1420+5252-12023	215.039520	52.891056	28.1	27.8	$7.13^{+0.11}_{-0.13}$	$-19.06^{+0.01}_{-0.01}$
beacon_1420+5252-7298	215.038239	52.877132	27.7	27.4	$7.13^{+0.11}_{-0.13}$	$-19.20^{+0.01}_{-0.01}$
beacon_1420+5252-9579	215.037079	52.892605	27.2	26.7	$7.14^{+0.10}_{-0.11}$	$-19.96^{+0.01}_{-0.01}$
beacon_1420+5252-3062	215.040863	52.863846	27.8	27.5	$7.14^{+0.12}_{-0.15}$	$-19.31^{+0.01}_{-0.01}$
beacon_1420+5252-10296	215.125000	52.874062	26.2	25.8	$7.16^{+0.11}_{-0.12}$	$-20.92^{+0.01}_{-0.01}$
beacon_0217-0504-6307	34.273205	-5.037470	28.2	27.1	$7.17^{+0.19}_{-0.17}$	$-18.82^{+0.02}_{-0.02}$
beacon_0217-0509-4631	34.241405	-5.150918	28.6	28.6	$7.18^{+0.45}_{-0.36}$	$-18.61^{+0.05}_{-0.06}$
beacon_0959+0200-14013	149.833344	2.036179	27.5	27.4	$7.18^{+0.23}_{-0.18}$	$-19.50^{+0.01}_{-0.01}$
beacon_1420+5252-12575	215.025375	52.891273	27.2	26.1	$7.18^{+0.05}_{-0.07}$	$-19.91^{+0.01}_{-0.01}$
beacon_0217-0504-2657	34.272232	-5.045108	28.9	27.6	$7.19^{+0.24}_{-0.12}$	$-18.14^{+0.01}_{-0.01}$
beacon_1420+5252-1569	214.994904	52.866634	27.6	27.3	$7.20^{+0.11}_{-0.19}$	$-19.54^{+0.01}_{-0.01}$
beacon_1138+5748-6058	174.370514	57.791782	26.8	26.0	$7.26^{+0.11}_{-0.11}$	$-20.25^{+0.01}_{-0.01}$
beacon_0959+0200-92	149.819672	1.965411	27.2	26.8	$7.29^{+0.16}_{-0.18}$	$-19.98^{+0.01}_{-0.01}$
beacon_0860+3857-14167	134.982468	38.985676	27.0	26.1	$7.29^{+1.05}_{-0.13}$	$-20.02^{+0.16}_{-0.01}$
beacon_0217-0508-8517	34.283566	-5.124747	29.1	29.0	$7.32^{+0.30}_{-0.13}$	$-17.94^{+0.01}_{-0.01}$
beacon_0332-2745-7700	53.071823	-27.782648	27.8	27.4	$7.34^{+0.49}_{-0.15}$	$-19.44^{+0.04}_{-0.01}$
beacon_0959+0200-1159	149.840607	1.964149	27.9	27.3	$7.34^{+0.14}_{-0.17}$	$-19.48^{+0.01}_{-0.01}$
beacon_0014-3025-10125	3.625879	-30.439075	-	27.9	$7.35^{+0.60}_{-0.07}$	$-18.52^{+0.08}_{-0.01}$
beacon_0332-2745-8900	53.053425	-27.765003	27.8	26.8	$7.35^{+0.08}_{-0.10}$	$-19.19^{+0.01}_{-0.01}$
beacon_1138+5748-3075	174.362335	57.780087	27.3	26.9	$7.37^{+0.54}_{-0.47}$	$-19.78^{+0.08}_{-0.06}$
beacon_1010+2701-3159	152.407913	27.005966	26.9	26.9	$7.38^{+0.29}_{-0.16}$	$-20.43^{+0.01}_{-0.01}$
beacon_0332-2745-15094	53.046597	-27.738073	27.3	27.5	$7.39^{+0.20}_{-0.15}$	$-19.79^{+0.01}_{-0.01}$
beacon_0332-2749-5025	53.086330	-27.823927	27.4	26.6	$7.39^{+0.35}_{-0.10}$	$-19.69^{+0.01}_{-0.01}$
beacon_0959+0200-1349	149.829239	1.969253	28.2	28.5	$7.39^{+0.43}_{-0.38}$	$-18.77^{+0.03}_{-0.04}$
beacon_0332-2745-13954	53.086193	-27.773207	28.6	28.4	$7.44^{+0.42}_{-0.36}$	$-18.70^{+0.04}_{-0.04}$

Table 3 *continued*

Table 3 (*continued*)

ID	R.A.	Decl.	m_{F150W}	m_{F444W}	z	M_{UV}
beacon_0217-0504-17278	34.329090	-5.092696	28.7	28.5	$7.45^{+0.53}_{-0.42}$	$-18.51^{+0.05}_{-0.06}$
beacon_0217-0504-6678	34.284660	-5.053731	29.0	29.0	$7.45^{+0.42}_{-0.35}$	$-18.18^{+0.04}_{-0.03}$
beacon_1420+5252-3630	215.084747	52.858551	27.7	27.6	$7.45^{+0.07}_{-0.08}$	$-19.72^{+0.01}_{-0.01}$
beacon_0217-0508-1040	34.320229	-5.164967	28.1	28.7	$7.48^{+0.45}_{-0.36}$	$-19.14^{+0.03}_{-0.04}$
beacon_0217-0504-10666	34.311810	-5.084851	28.0	26.8	$7.49^{+0.92}_{-0.23}$	$-19.31^{+0.08}_{-0.03}$
beacon_1420+5252-11406	215.110046	52.872971	28.5	28.6	$7.51^{+0.55}_{-0.47}$	$-18.77^{+0.05}_{-0.04}$
beacon_0217-0504-18177	34.323090	-5.081106	27.7	26.9	$7.51^{+0.73}_{-0.35}$	$-19.49^{+0.07}_{-0.04}$
beacon_0959+0200-13202	149.845184	2.029492	27.6	27.4	$7.53^{+0.43}_{-0.42}$	$-19.61^{+0.05}_{-0.04}$
beacon_0332-2745-10227	53.062523	-27.768053	28.2	27.5	$7.54^{+0.38}_{-0.50}$	$-19.11^{+0.05}_{-0.07}$
beacon_0332-2745-8698	53.053013	-27.765186	27.9	27.7	$7.56^{+0.48}_{-0.33}$	$-19.32^{+0.03}_{-0.03}$
beacon_0447-2637-2129	71.703773	-26.632273	27.1	26.5	$7.56^{+0.08}_{-0.07}$	$-19.97^{+0.01}_{-0.01}$
beacon_0217-0509-1974	34.221172	-5.180426	27.4	27.8	$7.57^{+0.22}_{-0.22}$	$-19.77^{+0.01}_{-0.01}$
beacon_0217-0509-6250	34.214062	-5.142040	28.4	28.2	$7.59^{+0.53}_{-0.46}$	$-18.80^{+0.04}_{-0.05}$
beacon_0217-0509-12575	34.207989	-5.121376	28.4	28.0	$7.65^{+0.37}_{-0.37}$	$-18.81^{+0.04}_{-0.03}$
beacon_0217-0509-85	34.234711	-5.188540	28.0	27.6	$7.65^{+0.55}_{-0.46}$	$-19.28^{+0.05}_{-0.06}$
beacon_0217-0509-1420	34.225983	-5.182612	28.6	28.1	$7.66^{+0.70}_{-0.59}$	$-18.65^{+0.08}_{-0.09}$
beacon_1420+5252-12428	215.084641	52.882202	27.9	26.9	$7.70^{+0.05}_{-0.05}$	$-19.54^{+0.01}_{-0.01}$
beacon_0217-0508-3329	34.318546	-5.148247	28.4	28.8	$7.71^{+0.47}_{-0.44}$	$-18.73^{+0.05}_{-0.04}$
beacon_0217-0504-6193	34.273129	-5.037531	28.3	27.6	$7.72^{+0.50}_{-0.46}$	$-19.04^{+0.05}_{-0.04}$
beacon_0014-3025-6550	3.572950	-30.413603	-	28.8	$7.77^{+0.63}_{-0.62}$	$-17.97^{+0.06}_{-0.07}$
beacon_0217-0508-8355	34.290524	-5.122096	28.8	28.8	$7.81^{+0.52}_{-0.54}$	$-18.25^{+0.05}_{-0.05}$
beacon_0332-2745-9353	53.022465	-27.739815	28.9	28.5	$7.82^{+0.46}_{-0.50}$	$-18.32^{+0.04}_{-0.04}$
beacon_0332-2745-15255	53.043163	-27.734766	29.0	27.8	$7.83^{+0.78}_{-0.77}$	$-18.30^{+0.11}_{-0.09}$
beacon_0217-0508-8334	34.286720	-5.123929	29.5	29.2	$7.84^{+0.70}_{-0.67}$	$-17.68^{+0.06}_{-0.07}$
beacon_0217-0508-14393	34.269173	-5.105772	28.1	26.8	$7.88^{+0.39}_{-0.44}$	$-19.06^{+0.05}_{-0.08}$
beacon_0014-3025-14457	3.608568	-30.418518	-	25.8	$7.90^{+0.19}_{-0.48}$	$-21.17^{+0.02}_{-0.02}$
beacon_0332-2745-18704	53.035835	-27.718058	28.5	28.0	$7.90^{+0.69}_{-0.77}$	$-18.72^{+0.07}_{-0.09}$
beacon_0217-0509-9363	34.219463	-5.127748	27.9	26.9	$7.90^{+0.33}_{-0.52}$	$-19.36^{+0.04}_{-0.06}$
beacon_0217-0509-2346	34.244049	-5.167047	29.2	28.5	$7.94^{+0.81}_{-0.81}$	$-18.08^{+0.09}_{-0.13}$
beacon_0217-0504-15163	34.292065	-5.043071	27.8	27.8	$7.96^{+0.31}_{-0.38}$	$-19.39^{+0.04}_{-0.01}$
beacon_0217-0504-10020	34.314068	-5.089706	28.3	26.3	$7.99^{+0.74}_{-0.83}$	$-18.77^{+0.12}_{-0.16}$
beacon_0217-0508-3572	34.296047	-5.156882	28.1	27.9	$8.03^{+0.46}_{-0.58}$	$-19.12^{+0.05}_{-0.04}$
beacon_0217-0508-1995	34.301559	-5.166206	27.4	26.6	$8.06^{+0.34}_{-0.36}$	$-19.94^{+0.03}_{-0.03}$
beacon_0217-0504-3421	34.270123	-5.040110	27.6	26.9	$8.06^{+0.33}_{-0.78}$	$-19.57^{+0.05}_{-0.05}$
beacon_0014-3025-2599	3.553823	-30.410107	-	28.1	$8.07^{+0.37}_{-0.57}$	$-18.68^{+0.04}_{-0.03}$
beacon_0959+0200-8926	149.829056	2.021058	27.9	26.5	$8.10^{+0.35}_{-0.21}$	$-19.38^{+0.03}_{-0.02}$
beacon_1420+5252-11933	215.035583	52.892235	25.2	24.7	$8.12^{+0.11}_{-0.12}$	$-22.05^{+0.01}_{-0.01}$
beacon_0217-0509-1475	34.246601	-5.172431	28.0	27.9	$8.12^{+0.41}_{-0.83}$	$-19.19^{+0.05}_{-0.06}$
beacon_0014-3025-8648	3.613551	-30.434706	-	27.2	$8.18^{+0.25}_{-0.25}$	$-19.70^{+0.01}_{-0.01}$
beacon_1010+2701-2444	152.446686	26.987419	27.2	26.6	$8.23^{+0.66}_{-1.00}$	$-20.08^{+0.06}_{-0.13}$
beacon_0217-0509-9252	34.209660	-5.132755	29.4	28.5	$8.24^{+0.75}_{-0.93}$	$-17.82^{+0.07}_{-0.09}$
beacon_1010+2701-19789	152.471619	27.051905	28.0	27.6	$8.26^{+0.61}_{-0.93}$	$-19.22^{+0.05}_{-0.05}$
beacon_0332-2745-17578	53.037659	-27.711735	27.3	26.5	$8.27^{+0.29}_{-1.02}$	$-20.08^{+0.01}_{-0.21}$
beacon_0332-2749-18718	53.058949	-27.808054	27.1	26.3	$8.27^{+0.17}_{-0.19}$	$-20.29^{+0.01}_{-0.01}$
beacon_1010+2701-16958	152.464661	27.046890	27.8	27.5	$8.28^{+0.61}_{-1.04}$	$-19.40^{+0.05}_{-0.12}$
beacon_0332-2749-24726	53.001209	-27.802843	26.8	25.3	$8.29^{+0.12}_{-0.13}$	$-20.74^{+0.02}_{-0.01}$

Table 3 *continued*

Table 3 (*continued*)

ID	R.A.	Decl.	m_{F150W}	m_{F444W}	z	M_{UV}
beacon_0217-0504-3873	34.314297	-5.105042	28.9	28.5	$8.30^{+0.51}_{-0.86}$	$-18.34^{+0.05}_{-0.06}$
beacon_0332-2745-8569	53.053482	-27.765987	28.3	27.8	$8.35^{+0.35}_{-0.40}$	$-18.83^{+0.02}_{-0.02}$
beacon_0217-0509-1793	34.224037	-5.180541	27.9	26.1	$8.39^{+0.26}_{-0.22}$	$-19.50^{+0.01}_{-0.01}$
beacon_0332-2745-8259	53.050213	-27.764677	27.0	26.3	$8.40^{+0.54}_{-0.35}$	$-20.29^{+0.06}_{-0.05}$
beacon_0217-0509-336	34.223042	-5.191769	26.0	24.9	$8.41^{+0.13}_{-0.13}$	$-21.52^{+0.01}_{-0.01}$
beacon_0217-0508-1427	34.307549	-5.168149	27.9	27.5	$8.41^{+0.26}_{-0.32}$	$-19.40^{+0.03}_{-0.01}$
beacon_0332-2745-17579	53.037807	-27.711599	26.7	26.5	$8.41^{+0.21}_{-0.22}$	$-20.63^{+0.01}_{-0.01}$
beacon_0332-2745-9828	53.012547	-27.731163	27.0	26.1	$8.42^{+0.14}_{-0.14}$	$-20.34^{+0.01}_{-0.01}$
beacon_0217-0508-9685	34.272381	-5.125317	28.9	28.8	$8.45^{+0.38}_{-0.57}$	$-18.46^{+0.03}_{-0.04}$
beacon_0014-3025-11608	3.612495	-30.427191	-	27.2	$8.47^{+0.22}_{-0.26}$	$-19.39^{+0.01}_{-0.01}$
beacon_0217-0509-435	34.222919	-5.191683	28.3	27.2	$8.49^{+0.30}_{-1.15}$	$-19.19^{+0.01}_{-0.32}$
beacon_0217-0509-6946	34.211567	-5.140682	28.2	27.4	$8.52^{+0.38}_{-0.45}$	$-19.12^{+0.05}_{-0.01}$
beacon_0217-0504-24295	34.306004	-5.045831	28.9	28.0	$8.52^{+0.65}_{-0.75}$	$-18.43^{+0.06}_{-0.07}$
beacon_0217-0508-3135	34.317574	-5.149925	28.5	27.8	$8.54^{+0.33}_{-0.40}$	$-18.88^{+0.02}_{-0.02}$
beacon_0217-0509-14993	34.214493	-5.112545	27.4	27.4	$8.56^{+0.23}_{-0.30}$	$-19.88^{+0.01}_{-0.01}$
beacon_0217-0509-13335	34.218163	-5.103996	28.3	27.9	$8.59^{+0.30}_{-0.40}$	$-19.13^{+0.02}_{-0.01}$
beacon_0217-0504-3515	34.270214	-5.040026	27.7	26.7	$8.63^{+0.17}_{-0.19}$	$-19.79^{+0.01}_{-0.01}$
beacon_0332-2749-12382	53.087475	-27.814884	27.3	26.0	$8.64^{+0.12}_{-0.16}$	$-20.18^{+0.01}_{-0.01}$
beacon_0217-0508-9763	34.272213	-5.124932	26.6	26.1	$8.68^{+0.14}_{-0.12}$	$-20.86^{+0.01}_{-0.01}$
beacon_0447-2637-11548	71.671661	-26.582500	27.3	27.6	$8.73^{+0.33}_{-0.29}$	$-19.97^{+0.01}_{-0.03}$
beacon_0217-0508-8040	34.302929	-5.117467	28.1	27.8	$8.75^{+0.28}_{-0.30}$	$-19.29^{+0.02}_{-0.01}$
beacon_0217-0508-8415	34.292923	-5.120759	28.4	28.6	$8.77^{+0.31}_{-0.40}$	$-18.84^{+0.03}_{-0.01}$
beacon_0860+3857-14145	134.982574	38.985649	26.3	25.7	$8.79^{+0.19}_{-0.21}$	$-21.08^{+0.01}_{-0.01}$
beacon_0014-3025-10503	3.624762	-30.437508	-	27.0	$8.81^{+0.16}_{-0.17}$	$-20.22^{+0.01}_{-0.01}$
beacon_0217-0509-4602	34.220940	-5.160698	27.3	26.2	$8.82^{+0.25}_{-0.16}$	$-20.12^{+0.02}_{-0.01}$
beacon_1010+2701-420	152.422150	26.986328	26.0	24.7	$8.87^{+0.31}_{-0.25}$	$-21.44^{+0.04}_{-0.03}$
beacon_0217-0508-12114	34.277187	-5.113205	28.3	27.0	$8.92^{+0.25}_{-0.23}$	$-19.21^{+0.01}_{-0.01}$
beacon_0217-0509-11648	34.212341	-5.122705	27.7	27.2	$8.98^{+0.21}_{-0.20}$	$-19.57^{+0.01}_{-0.01}$
beacon_1420+5252-2768	215.008652	52.868328	26.4	26.4	$9.04^{+0.14}_{-0.15}$	$-21.05^{+0.01}_{-0.01}$
beacon_0217-0504-10016	34.283627	-5.044103	28.0	27.9	$9.07^{+0.24}_{-0.22}$	$-19.42^{+0.01}_{-0.01}$
beacon_0959+0200-16783	149.836929	2.041479	26.9	27.2	$9.14^{+0.17}_{-0.21}$	$-20.52^{+0.01}_{-0.01}$
beacon_0217-0504-7157	34.309956	-5.090462	26.9	27.7	$9.16^{+0.15}_{-0.15}$	$-20.28^{+0.01}_{-0.02}$
beacon_0217-0509-14115	34.200089	-5.116339	28.7	29.7	$9.25^{+0.09}_{-0.38}$	$-18.55^{+0.01}_{-0.01}$
beacon_1010+2701-18712	152.439987	27.060465	26.9	25.9	$9.31^{+1.60}_{-0.42}$	$-20.63^{+0.24}_{-0.10}$
beacon_0217-0508-1490	34.314037	-5.164579	28.3	28.1	$9.38^{+0.34}_{-0.55}$	$-19.25^{+0.01}_{-0.06}$
beacon_0217-0508-3296	34.305820	-5.154357	27.3	27.5	$9.40^{+0.28}_{-0.16}$	$-20.14^{+0.01}_{-0.01}$
beacon_0014-3025-13872	3.617229	-30.425524	-	26.0	$9.48^{+0.08}_{-0.08}$	$-21.69^{+0.01}_{-0.01}$
beacon_0217-0504-9016	34.283463	-5.046202	28.2	28.0	$9.52^{+1.32}_{-1.57}$	$-19.19^{+0.15}_{-0.52}$
beacon_0217-0509-2696	34.237087	-5.1677516	27.6	27.2	$9.52^{+1.34}_{-1.46}$	$-19.82^{+0.15}_{-0.54}$
beacon_1010+2701-17114	152.439484	27.056280	26.5	26.0	$9.67^{+1.26}_{-0.22}$	$-21.42^{+0.07}_{-0.18}$
beacon_0332-2749-16743	53.001728	-27.812489	28.1	27.7	$9.79^{+0.57}_{-0.26}$	$-19.75^{+0.04}_{-0.01}$
beacon_0442-4613-8264	70.427460	-46.230682	26.2	26.9	$9.83^{+0.69}_{-0.99}$	$-21.02^{+0.04}_{-0.07}$
beacon_0217-0508-7634	34.305424	-5.118019	28.5	28.7	$9.91^{+0.78}_{-0.72}$	$-18.92^{+0.05}_{-0.06}$
beacon_0860+3857-10356	134.977585	38.971680	27.5	26.5	$9.99^{+1.22}_{-0.97}$	$-19.98^{+0.14}_{-0.18}$
beacon_0217-0509-12959	34.221210	-5.113707	29.0	28.6	$10.02^{+1.11}_{-1.03}$	$-18.62^{+0.08}_{-0.13}$
beacon_0217-0508-11070	34.298710	-5.107352	27.8	27.8	$10.04^{+0.61}_{-1.03}$	$-19.66^{+0.06}_{-0.07}$

Table 3 *continued*

Table 3 (*continued*)

ID	R.A.	Decl.	m_{F150W}	m_{F444W}	z	M_{UV}
beacon_0332-2749-19513	53.075996	-27.806505	27.8	28.0	$10.13^{+0.42}_{-0.43}$	$-19.74^{+0.01}_{-0.02}$
beacon_1138+5748-2321	174.362198	57.776512	27.1	26.3	$10.17^{+1.36}_{-1.31}$	$-20.52^{+0.15}_{-0.15}$
beacon_0332-2749-17529	53.085506	-27.808601	27.7	28.0	$10.24^{+0.67}_{-0.62}$	$-19.90^{+0.03}_{-0.04}$
beacon_0217-0509-13052	34.221394	-5.113218	28.1	28.4	$10.26^{+0.45}_{-0.61}$	$-19.49^{+0.04}_{-0.02}$
beacon_0217-0509-11058	34.217091	-5.122624	28.7	27.3	$10.32^{+1.12}_{-1.11}$	$-18.84^{+0.13}_{-0.17}$
beacon_1010+2701-12141	152.432724	27.044855	28.4	26.7	$10.75^{+0.98}_{-1.30}$	$-19.34^{+0.12}_{-0.08}$
beacon_0959+0200-14138	149.845947	2.032689	28.2	27.5	$11.04^{+0.44}_{-0.38}$	$-19.57^{+0.03}_{-0.01}$
beacon_0332-2745-18596	53.085110	-27.757654	28.2	27.8	$11.22^{+0.70}_{-0.70}$	$-20.07^{+0.04}_{-0.04}$
beacon_0332-2749-6608	53.005013	-27.824554	29.3	27.8	$12.29^{+2.46}_{-1.19}$	$-19.64^{+0.24}_{-0.14}$

NOTE—Sources are sorted in increased order of redshift.

REFERENCES

- Adams, N. J., Conselice, C. J., Austin, D., et al. 2024, ApJ, 965, 169, doi: [10.3847/1538-4357/ad2a7b](https://doi.org/10.3847/1538-4357/ad2a7b)
- Arrabal Haro, P., Dickinson, M., Finkelstein, S. L., et al. 2023, arXiv e-prints, arXiv:2304.05378, doi: [10.48550/arXiv.2304.05378](https://doi.org/10.48550/arXiv.2304.05378)
- Astropy Collaboration, Robitaille, T. P., Tollerud, E. J., et al. 2013, A&A, 558, A33, doi: [10.1051/0004-6361/201322068](https://doi.org/10.1051/0004-6361/201322068)
- Astropy Collaboration, Price-Whelan, A. M., Sipőcz, B. M., et al. 2018, AJ, 156, 123, doi: [10.3847/1538-3881/aabc4f](https://doi.org/10.3847/1538-3881/aabc4f)
- Astropy Collaboration, Price-Whelan, A. M., Lim, P. L., et al. 2022, ApJ, 935, 167, doi: [10.3847/1538-4357/ac7c74](https://doi.org/10.3847/1538-4357/ac7c74)
- Atek, H., Siana, B., Scarlata, C., et al. 2011, ApJ, 743, 121, doi: [10.1088/0004-637X/743/2/121](https://doi.org/10.1088/0004-637X/743/2/121)
- Bagley, M. B., Finkelstein, S. L., Koekemoer, A. M., et al. 2023, ApJL, 946, L12, doi: [10.3847/2041-8213/acbb08](https://doi.org/10.3847/2041-8213/acbb08)
- Barro, G., Faber, S. M., Koo, D. C., et al. 2017, ApJ, 840, 47, doi: [10.3847/1538-4357/aa6b05](https://doi.org/10.3847/1538-4357/aa6b05)
- Barrufet, L., Oesch, P., Marques-Chaves, R., et al. 2024, arXiv e-prints, arXiv:2404.08052, doi: [10.48550/arXiv.2404.08052](https://doi.org/10.48550/arXiv.2404.08052)
- Behroozi, P., Wechsler, R., Hearn, A., & Conroy, C. 2018, ArXiv e-prints. <https://arxiv.org/abs/1806.07893>
- Bernard, S. R., Carrasco, D., Trenti, M., et al. 2016, ApJ, 827, 76, doi: [10.3847/0004-637X/827/1/76](https://doi.org/10.3847/0004-637X/827/1/76)
- Bertin, E., & Arnouts, S. 1996, A&AS, 117, 393
- Bhowmick, A. K., Somerville, R. S., Di Matteo, T., et al. 2020, MNRAS, 496, 754, doi: [10.1093/mnras/staa1605](https://doi.org/10.1093/mnras/staa1605)
- Boucaud, A., Bocchio, M., Abergel, A., et al. 2016, A&A, 596, A63, doi: [10.1051/0004-6361/201629080](https://doi.org/10.1051/0004-6361/201629080)
- Bouwens, R., Illingworth, G., Oesch, P., et al. 2022, arXiv e-prints, arXiv:2212.06683. <https://arxiv.org/abs/2212.06683>
- Bouwens, R. J., Stefanon, M., Oesch, P. A., et al. 2019, ApJ, 880, 25, doi: [10.3847/1538-4357/ab24c5](https://doi.org/10.3847/1538-4357/ab24c5)
- Bouwens, R. J., Illingworth, G. D., Oesch, P. A., et al. 2010, ApJL, 709, L133, doi: [10.1088/2041-8205/709/2/L133](https://doi.org/10.1088/2041-8205/709/2/L133)
- . 2015, ApJ, 803, 34, doi: [10.1088/0004-637X/803/1/34](https://doi.org/10.1088/0004-637X/803/1/34)
- Bouwens, R. J., Oesch, P. A., Stefanon, M., et al. 2021, AJ, 162, 47, doi: [10.3847/1538-3881/abf83e](https://doi.org/10.3847/1538-3881/abf83e)
- Bowler, R. A. A., Jarvis, M. J., Dunlop, J. S., et al. 2020, MNRAS, 493, 2059, doi: [10.1093/mnras/staa313](https://doi.org/10.1093/mnras/staa313)
- Bowler, R. A. A., Dunlop, J. S., McLure, R. J., et al. 2014, MNRAS, 440, 2810, doi: [10.1093/mnras/stu449](https://doi.org/10.1093/mnras/stu449)
- Boylan-Kolchin, M. 2022, arXiv e-prints, arXiv:2208.01611. <https://arxiv.org/abs/2208.01611>
- Bradley, L. 2023, larrybradley/lacosmic: 1.1.0, 1.1.0, Zenodo, doi: [10.5281/zenodo.1014563](https://doi.org/10.5281/zenodo.1014563)
- Bradley, L. D., Trenti, M., Oesch, P. A., et al. 2012, ApJ, 760, 108, doi: [10.1088/0004-637X/760/2/108](https://doi.org/10.1088/0004-637X/760/2/108)
- Brammer, G., Strait, V., Matharu, J., & Momcheva, I. 2022, grizli, 1.5.0, Zenodo, Zenodo, doi: [10.5281/zenodo.6672538](https://doi.org/10.5281/zenodo.6672538)
- Brammer, G. B., van Dokkum, P. G., & Coppi, P. 2008, ApJ, 686, 1503, doi: [10.1086/591786](https://doi.org/10.1086/591786)
- Bridge, J. S., Holwerda, B. W., Stefanon, M., et al. 2019, ApJ, 882, 42, doi: [10.3847/1538-4357/ab3213](https://doi.org/10.3847/1538-4357/ab3213)
- Bunker, A. J., Stanway, E. R., Ellis, R. S., & McMahon, R. G. 2004, MNRAS, 355, 374, doi: [10.1111/j.1365-2966.2004.08326.x](https://doi.org/10.1111/j.1365-2966.2004.08326.x)

Table 4. Columns and description for the photometric catalogs.

Column	Unit	Description
Photometric Catalog		
id		Individual identification name of objects.
ra	degree	R.A. (J2000).
dec	degree	Declination (J2000).
x	pixel	x position in image coordinate.
y	pixel	y position in image coordinate.
f_xx	f_ν	Total flux of objects in band xx.
e_xx	f_ν	Flux error (1σ) in total flux of objects in band xx.
flux_iso_xx	f_ν	Isophotal flux in band xx.
fluxerr_iso_xx	f_ν	Flux error (1σ) in isophotal flux in band xx.
flux_aper_n_xx	f_ν	Aperture flux in band xx in the n th aperture. Aperture diameter sizes are: [0.16, 0.32, 0.48, 0.64, 1.28, 2.56] arcsec.
flux_aper_n_xx	f_ν	Flux error (1σ) in aperture flux in band xx in the n th aperture.
flag_xx		SExtractor photometry flag for band xx.
kron_radius_xx	pixel	Kron radius in band xx.
a_image_xx	pixel	Radius along the major axis in band xx.
b_image_xx	pixel	Radius along the minor axis in band xx.
theta_xx	degree	SExtractor position angle in band xx measured counterclockwise.
class_star_xx		SExtractor class star indicator in band xx.
flux_radius_xx	pixel	SExtractor Non-parametric half-light radius in band xx.
flux_scale		Scale ratio of total flux to aperture flux measured in the detection band. The minimum scale is set to 1.
Redshift catalog		
zn		Photometric redshift at the n th percentile of redshift likelihood distribution.
zpeak		Photometric redshift at the peak of global likelihood redshift distribution.
chi2		Reduced chi-square at zpeak.
MUVn	mag	Absolute UV (1450 Å) magnitude calculated at zn.
MUVpeak	mag	Absolute UV (1450 Å) magnitude calculated at zpeak.
plow		Total probability of redshift distribution at $z < z_{\text{set}}$.
phigh		Total probability of redshift distribution at $z > z_{\text{set}}$.
UVbeta_lambda		UV-beta slope (β_λ) calculated with the best-fit template at zpeak.
U-V	mag	Rest-frame U - V color calculated with the best-fit template at zpeak.
B-V	mag	Rest-frame B - V color calculated with the best-fit template at zpeak.
V-J	mag	Rest-frame V - J color calculated with the best-fit template at zpeak.
z-J	mag	Rest-frame z - J color calculated with the best-fit template at zpeak.
z_peak_low		Photometric redshift at the peak of redshift likelihood distribution at $z < z_{\text{set}}$.
chi2_peak_low		Reduced chi-square at z_peak_low.
z_peak_high		Photometric redshift at the peak of redshift likelihood distribution at $z > z_{\text{set}}$.
chi2_peak_high		Reduced chi-square at z_peak_high.
nfilt		Number of filters used for photometric redshift fit.

NOTE—All fluxes are corrected for the Galactic dust extinction, and set to magnitude zeropoint of $m_0 = 25$ i.e. $m = -2.5 \log(f_\nu) + m_0$. For sources with filters without data coverage, the flux error arrays are set to -99.

- Bunker, A. J., Wilkins, S., Ellis, R. S., et al. 2010, MNRAS, 409, 855, doi: [10.1111/j.1365-2966.2010.17350.x](https://doi.org/10.1111/j.1365-2966.2010.17350.x)
- Bunker, A. J., Saxena, A., Cameron, A. J., et al. 2023, A&A, 677, A88, doi: [10.1051/0004-6361/202346159](https://doi.org/10.1051/0004-6361/202346159)
- Burgasser, A. J., Bezanson, R., Labbe, I., et al. 2024, ApJ, 962, 177, doi: [10.3847/1538-4357/ad206f](https://doi.org/10.3847/1538-4357/ad206f)
- Calvi, V., Trenti, M., Stiavelli, M., et al. 2016, ApJ, 817, 120, doi: [10.3847/0004-637X/817/2/120](https://doi.org/10.3847/0004-637X/817/2/120)
- Cameron, A. J., Trenti, M., Livermore, R. C., & van der Velden, C. 2019, MNRAS, 483, 1922, doi: [10.1093/mnras/sty3069](https://doi.org/10.1093/mnras/sty3069)
- Cardelli, J. A., Clayton, G. C., & Mathis, J. S. 1989, ApJ, 345, 245, doi: [10.1086/167900](https://doi.org/10.1086/167900)
- Carnall, A. C., McLeod, D. J., McLure, R. J., et al. 2022, arXiv e-prints, arXiv:2208.00986. <https://arxiv.org/abs/2208.00986>
- Carnall, A. C., McLure, R. J., Dunlop, J. S., et al. 2023, Nature, 619, 716, doi: [10.1038/s41586-023-06158-6](https://doi.org/10.1038/s41586-023-06158-6)
- Carniani, S., Hainline, K., D'Eugenio, F., et al. 2024, Nature, 633, 318, doi: [10.1038/s41586-024-07860-9](https://doi.org/10.1038/s41586-024-07860-9)
- Casey, C. M., Kartaltepe, J. S., Drakos, N. E., et al. 2022, arXiv e-prints, arXiv:2211.07865, doi: [10.48550/arXiv.2211.07865](https://doi.org/10.48550/arXiv.2211.07865)
- Casey, C. M., Akins, H. B., Shuntov, M., et al. 2023, arXiv e-prints, arXiv:2308.10932, doi: [10.48550/arXiv.2308.10932](https://doi.org/10.48550/arXiv.2308.10932)
- Castellano, M., Fontana, A., Treu, T., et al. 2022, ApJL, 938, L15, doi: [10.3847/2041-8213/ac94d0](https://doi.org/10.3847/2041-8213/ac94d0)
- Castellano, M., Napolitano, L., Fontana, A., et al. 2024, ApJ, 972, 143, doi: [10.3847/1538-4357/ad5f88](https://doi.org/10.3847/1538-4357/ad5f88)
- Chabrier, G. 2003, PASP, 115, 763, doi: [10.1086/376392](https://doi.org/10.1086/376392)
- Champagne, J. B., Wang, F., Yang, J., et al. 2024, arXiv e-prints, arXiv:2410.03827, doi: [10.48550/arXiv.2410.03827](https://doi.org/10.48550/arXiv.2410.03827)
- Chen, Z., Stark, D. P., Endsley, R., et al. 2023, MNRAS, 518, 5607, doi: [10.1093/mnras/stac3476](https://doi.org/10.1093/mnras/stac3476)
- Conroy, C., Gunn, J. E., & White, M. 2009, ApJ, 699, 486, doi: [10.1088/0004-637X/699/1/486](https://doi.org/10.1088/0004-637X/699/1/486)
- Curtis-Lake, E., Carniani, S., Cameron, A., et al. 2022, arXiv e-prints, arXiv:2212.04568. <https://arxiv.org/abs/2212.04568>
- . 2023, Nature Astronomy, 7, 622, doi: [10.1038/s41550-023-01918-w](https://doi.org/10.1038/s41550-023-01918-w)
- Daddi, E., Renzini, A., Pirzkal, N., et al. 2005, ApJ, 626, 680, doi: [10.1086/430104](https://doi.org/10.1086/430104)
- Damjanov, I., McCarthy, P. J., Abraham, R. G., et al. 2009, ApJ, 695, 101, doi: [10.1088/0004-637X/695/1/101](https://doi.org/10.1088/0004-637X/695/1/101)
- Davidzon, I., Ilbert, O., Laigle, C., et al. 2017, A&A, 605, A70, doi: [10.1051/0004-6361/201730419](https://doi.org/10.1051/0004-6361/201730419)
- Dayal, P., Ferrara, A., Dunlop, J. S., & Pacucci, F. 2014, MNRAS, 445, 2545, doi: [10.1093/mnras/stu1848](https://doi.org/10.1093/mnras/stu1848)
- de Graaff, A., Setton, D. J., Brammer, G., et al. 2024, arXiv e-prints, arXiv:2404.05683, doi: [10.48550/arXiv.2404.05683](https://doi.org/10.48550/arXiv.2404.05683)
- Donnan, C. T., McLeod, D. J., Dunlop, J. S., et al. 2022, arXiv:2207.12356. <https://arxiv.org/abs/2207.12356>
- Donnan, C. T., McLure, R. J., Dunlop, J. S., et al. 2024, MNRAS, 533, 3222, doi: [10.1093/mnras/stae2037](https://doi.org/10.1093/mnras/stae2037)
- Ellis, R. S., McLure, R. J., Dunlop, J. S., et al. 2013, ApJL, 763, L7, doi: [10.1088/2041-8205/763/1/L7](https://doi.org/10.1088/2041-8205/763/1/L7)
- Elmegreen, B. G., & Elmegreen, D. M. 2005, ApJ, 627, 632, doi: [10.1086/430514](https://doi.org/10.1086/430514)
- Endsley, R., Stark, D. P., Whitler, L., et al. 2022, arXiv e-prints, arXiv:2208.14999. <https://arxiv.org/abs/2208.14999>
- Ferreira, L., Adams, N., Conselice, C. J., et al. 2022, ApJL, 938, L2, doi: [10.3847/2041-8213/ac947c](https://doi.org/10.3847/2041-8213/ac947c)
- Finkelstein, S. L., Bagley, M. B., Haro, P. A., et al. 2022, ApJL, 940, L55, doi: [10.3847/2041-8213/ac966e](https://doi.org/10.3847/2041-8213/ac966e)
- Foreman-Mackey, D., Hogg, D. W., Lang, D., & Goodman, J. 2013, PASP, 125, 306, doi: [10.1086/670067](https://doi.org/10.1086/670067)
- Förster Schreiber, N. M., Genzel, R., Bouché, N., et al. 2009, ApJ, 706, 1364, doi: [10.1088/0004-637X/706/2/1364](https://doi.org/10.1088/0004-637X/706/2/1364)
- Franco, M., Akins, H. B., Casey, C. M., et al. 2024, ApJ, 973, 23, doi: [10.3847/1538-4357/ad5e6a](https://doi.org/10.3847/1538-4357/ad5e6a)
- Fudamoto, Y., Inoue, A. K., & Sugahara, Y. 2022, ApJL, 938, L24, doi: [10.3847/2041-8213/ac982b](https://doi.org/10.3847/2041-8213/ac982b)
- Fukugita, M., Ichikawa, T., Gunn, J. E., et al. 1996, AJ, 111, 1748, doi: [10.1086/117915](https://doi.org/10.1086/117915)
- Gehrels, N. 1986, ApJ, 303, 336, doi: [10.1086/164079](https://doi.org/10.1086/164079)
- Gelli, V., Mason, C., & Hayward, C. C. 2024, arXiv e-prints, arXiv:2405.13108, doi: [10.48550/arXiv.2405.13108](https://doi.org/10.48550/arXiv.2405.13108)
- Genzel, R., Newman, S., Jones, T., et al. 2011, ApJ, 733, 101, doi: [10.1088/0004-637X/733/2/101](https://doi.org/10.1088/0004-637X/733/2/101)
- Glazebrook, K., Schreiber, C., Labb , I., et al. 2017, Nature, 544, 71, doi: [10.1038/nature21680](https://doi.org/10.1038/nature21680)
- Glazebrook, K., Nanayakkara, T., Schreiber, C., et al. 2023, arXiv e-prints, arXiv:2308.05606, doi: [10.48550/arXiv.2308.05606](https://doi.org/10.48550/arXiv.2308.05606)
- . 2024, Nature, 628, 277, doi: [10.1038/s41586-024-07191-9](https://doi.org/10.1038/s41586-024-07191-9)
- Greene, J. E., Labbe, I., Goulding, A. D., et al. 2023, arXiv e-prints, arXiv:2309.05714, doi: [10.48550/arXiv.2309.05714](https://doi.org/10.48550/arXiv.2309.05714)
- Grogan, N. A., Kocevski, D. D., Faber, S. M., et al. 2011, ApJS, 197, 35, doi: [10.1088/0067-0049/197/2/35](https://doi.org/10.1088/0067-0049/197/2/35)
- Guo, K., Zheng, X. Z., Wang, T., & Fu, H. 2015, ApJL, 808, L49, doi: [10.1088/2041-8205/808/2/L49](https://doi.org/10.1088/2041-8205/808/2/L49)

- Guo, Y., Jogee, S., Finkelstein, S. L., et al. 2022, arXiv e-prints, arXiv:2210.08658.
<https://arxiv.org/abs/2210.08658>
- Hainline, K. N., Johnson, B. D., Robertson, B., et al. 2023, arXiv e-prints, arXiv:2306.02468, doi: 10.48550/arXiv.2306.02468
- Hainline, K. N., Helton, J. M., Johnson, B. D., et al. 2024, ApJ, 964, 66, doi: 10.3847/1538-4357/ad20d1
- Harikane, Y., Nakajima, K., Ouchi, M., et al. 2023a, arXiv e-prints, arXiv:2304.06658, doi: 10.48550/arXiv.2304.06658
- Harikane, Y., Ouchi, M., Oguri, M., et al. 2022, arXiv e-prints, arXiv:2208.01612.
<https://arxiv.org/abs/2208.01612>
- Harikane, Y., Zhang, Y., Nakajima, K., et al. 2023b, arXiv e-prints, arXiv:2303.11946, doi: 10.48550/arXiv.2303.11946
- Harris, C. R., Millman, K. J., van der Walt, S. J., et al. 2020, Nature, 585, 357, doi: 10.1038/s41586-020-2649-2
- Holwerda, B. W., Trenti, M., Clarkson, W., et al. 2014, ApJ, 788, 77, doi: 10.1088/0004-637X/788/1/77
- Holwerda, B. W., Bridge, J. S., Ryan, R., et al. 2018, A&A, 620, A132, doi: 10.1051/0004-6361/201832838
- Illingworth, G. D., Magee, D., Oesch, P. A., et al. 2013, ApJS, 209, 6, doi: 10.1088/0067-0049/209/1/6
- Inami, H., Armus, L., Matsuhara, H., et al. 2018, A&A, 617, A130, doi: 10.1051/0004-6361/201833053
- Ishigaki, M., Kawamata, R., Ouchi, M., et al. 2018, ApJ, 854, 73, doi: 10.3847/1538-4357/aaa544
- Ishikawa, Y., Morishita, T., Stiavelli, M., et al. 2022, ApJ, 936, 167, doi: 10.3847/1538-4357/ac8874
- Ito, K., Valentino, F., Brammer, G., et al. 2023, arXiv e-prints, arXiv:2307.06994, doi: 10.48550/arXiv.2307.06994
- Jarosik, N., Bennett, C. L., Dunkley, J., et al. 2011, ApJS, 192, 14, doi: 10.1088/0067-0049/192/2/14
- Jung, I., Finkelstein, S. L., Larson, R. L., et al. 2022, arXiv e-prints, arXiv:2212.09850, doi: 10.48550/arXiv.2212.09850
- Kannan, R., Garaldi, E., Smith, A., et al. 2022, MNRAS, 511, 4005, doi: 10.1093/mnras/stab3710
- Katz, H., Cameron, A. J., Saxena, A., et al. 2024, arXiv e-prints, arXiv:2408.03189, doi: 10.48550/arXiv.2408.03189
- Kocevski, D. D., Onoue, M., Inayoshi, K., et al. 2023, arXiv e-prints, arXiv:2302.00012, doi: 10.48550/arXiv.2302.00012
- Koekemoer, A. M., Faber, S. M., Ferguson, H. C., et al. 2011, ApJS, 197, 36, doi: 10.1088/0067-0049/197/2/36
- Kokubo, M., & Harikane, Y. 2024, arXiv e-prints, arXiv:2407.04777, doi: 10.48550/arXiv.2407.04777
- Labbe, I., Greene, J. E., Bezanson, R., et al. 2023, arXiv e-prints, arXiv:2306.07320, doi: 10.48550/arXiv.2306.07320
- Larson, R. L., Finkelstein, S. L., Hutchison, T. A., et al. 2022, ApJ, 930, 104, doi: 10.3847/1538-4357/ac5dbd
- Larson, R. L., Finkelstein, S. L., Kocevski, D. D., et al. 2023, arXiv e-prints, arXiv:2303.08918, doi: 10.48550/arXiv.2303.08918
- Leethochawalit, N., Roberts-Borsani, G., Morishita, T., Trenti, M., & Treu, T. 2023, MNRAS, 524, 5454, doi: 10.1093/mnras/stad2202
- Leethochawalit, N., Trenti, M., Santini, P., et al. 2022, arXiv e-prints, arXiv:2207.11135.
<https://arxiv.org/abs/2207.11135>
- Leung, G. C. K., Bagley, M. B., Finkelstein, S. L., et al. 2023, ApJL, 954, L46, doi: 10.3847/2041-8213/acf365
- Livermore, R. C., Trenti, M., Bradley, L. D., et al. 2018, ApJL, 861, L17, doi: 10.3847/2041-8213/aacd16
- Llerena, M., Amorín, R., Pentericci, L., et al. 2024, arXiv e-prints, arXiv:2403.05362, doi: 10.48550/arXiv.2403.05362
- Lovell, C. C., Harrison, I., Harikane, Y., Tacchella, S., & Wilkins, S. M. 2023, MNRAS, 518, 2511, doi: 10.1093/mnras/stac3224
- Madau, P., Ferguson, H. C., Dickinson, M. E., et al. 1996, MNRAS, 283, 1388
- Mashian, N., Oesch, P. A., & Loeb, A. 2016, MNRAS, 455, 2101, doi: 10.1093/mnras/stv2469
- Mason, C. A., Trenti, M., & Treu, T. 2022, arXiv e-prints, arXiv:2207.14808. <https://arxiv.org/abs/2207.14808>
—. 2023, MNRAS, 521, 497, doi: 10.1093/mnras/stad035
- Mason, C. A., Treu, T., Schmidt, K. B., et al. 2015, ApJ, 805, 79, doi: 10.1088/0004-637X/805/1/79
- Matthee, J., Naidu, R. P., Brammer, G., et al. 2023, arXiv e-prints, arXiv:2306.05448, doi: 10.48550/arXiv.2306.05448
- McLeod, D. J., Donnan, C. T., McLure, R. J., et al. 2024, MNRAS, 527, 5004, doi: 10.1093/mnras/stad3471
- Morishita, T. 2021, ApJS, 253, 4, doi: 10.3847/1538-4365/abce67
- Morishita, T. 2023, mtakahiro/bbpm: v1.3, v1.3, Zenodo, doi: 10.5281/zenodo.10067906
- Morishita, T., & Stiavelli, M. 2023, ApJL, 946, L35, doi: 10.3847/2041-8213/acbf50
- Morishita, T., Trenti, M., Stiavelli, M., et al. 2018, ApJ, 867, 150, doi: 10.3847/1538-4357/aae68c
- Morishita, T., Stiavelli, M., Trenti, M., et al. 2020, ApJ, 904, 50, doi: 10.3847/1538-4357/abba83

- Morishita, T., Roberts-Borsani, G., Treu, T., et al. 2023, ApJL, 947, L24, doi: [10.3847/2041-8213/acb99e](https://doi.org/10.3847/2041-8213/acb99e)
- Morishita, T., Liu, Z., Stiavelli, M., et al. 2024a, arXiv e-prints, arXiv:2408.10980, doi: [10.48550/arXiv.2408.10980](https://doi.org/10.48550/arXiv.2408.10980)
- Morishita, T., Stiavelli, M., Chary, R.-R., et al. 2024b, ApJ, 963, 9, doi: [10.3847/1538-4357/ad1404](https://doi.org/10.3847/1538-4357/ad1404)
- Naidu, R. P., Oesch, P. A., Dokkum, P. v., et al. 2022, ApJL, 940, L14, doi: [10.3847/2041-8213/ac9b22](https://doi.org/10.3847/2041-8213/ac9b22)
- Nanayakkara, T., Glazebrook, K., Jacobs, C., et al. 2024, Scientific Reports, 14, 3724, doi: [10.1038/s41598-024-52585-4](https://doi.org/10.1038/s41598-024-52585-4)
- Napolitano, L., Castellano, M., Pentericci, L., et al. 2024, arXiv e-prints, arXiv:2410.10967, doi: [10.48550/arXiv.2410.10967](https://doi.org/10.48550/arXiv.2410.10967)
- Newman, A. B., Ellis, R. S., Andreon, S., et al. 2014, ApJ, 788, 51, doi: [10.1088/0004-637X/788/1/51](https://doi.org/10.1088/0004-637X/788/1/51)
- Nonino, M., Glazebrook, K., Burgasser, A. J., et al. 2022, arXiv e-prints, arXiv:2207.14802, <https://arxiv.org/abs/2207.14802>
- Oesch, P. A., Bouwens, R. J., Illingworth, G. D., Labb  , I., & Stefanon, M. 2018, ApJ, 855, 105, doi: [10.3847/1538-4357/aab03f](https://doi.org/10.3847/1538-4357/aab03f)
- Oesch, P. A., Bouwens, R. J., Illingworth, G. D., et al. 2010, ApJL, 709, L16, doi: [10.1088/2041-8205/709/1/L16](https://doi.org/10.1088/2041-8205/709/1/L16)
- . 2013, ApJ, 773, 75, doi: [10.1088/0004-637X/773/1/75](https://doi.org/10.1088/0004-637X/773/1/75)
- Oke, J. B., & Gunn, J. E. 1983, ApJ, 266, 713, doi: [10.1086/160817](https://doi.org/10.1086/160817)
- Onoue, M., Inayoshi, K., Ding, X., et al. 2023, ApJL, 942, L17, doi: [10.3847/2041-8213/aca9d3](https://doi.org/10.3847/2041-8213/aca9d3)
- Rayner, J. T., Toomey, D. W., Onaka, P. M., et al. 2003, PASP, 115, 362, doi: [10.1086/367745](https://doi.org/10.1086/367745)
- Ren, K., Trenti, M., & Mason, C. A. 2019, ApJ, 878, 114, doi: [10.3847/1538-4357/ab2117](https://doi.org/10.3847/1538-4357/ab2117)
- Roberts-Borsani, G., Morishita, T., Treu, T., Leethochawalit, N., & Trenti, M. 2022, ApJ, 927, 236, doi: [10.3847/1538-4357/ac4803](https://doi.org/10.3847/1538-4357/ac4803)
- Roberts-Borsani, G., Bagley, M., Rojas-Ruiz, S., et al. 2024a, arXiv e-prints, arXiv:2407.17551, doi: [10.48550/arXiv.2407.17551](https://doi.org/10.48550/arXiv.2407.17551)
- Roberts-Borsani, G., Treu, T., Shapley, A., et al. 2024b, arXiv e-prints, arXiv:2403.07103, doi: [10.48550/arXiv.2403.07103](https://doi.org/10.48550/arXiv.2403.07103)
- Roberts-Borsani, G. W., Bouwens, R. J., Oesch, P. A., et al. 2016, ApJ, 823, 143, doi: [10.3847/0004-637X/823/2/143](https://doi.org/10.3847/0004-637X/823/2/143)
- Robertson, B., Johnson, B. D., Tacchella, S., et al. 2024, ApJ, 970, 31, doi: [10.3847/1538-4357/ad463d](https://doi.org/10.3847/1538-4357/ad463d)
- Robertson, B. E. 2010, ApJL, 716, L229, doi: [10.1088/2041-8205/716/2/L229](https://doi.org/10.1088/2041-8205/716/2/L229)
- Rojas-Ruiz, S., Finkelstein, S. L., Bagley, M. B., et al. 2020, arXiv e-prints, arXiv:2002.06209, <https://arxiv.org/abs/2002.06209>
- Rojas-Ruiz, S., Bagley, M. B., Roberts-Borsani, G., et al. 2024, arXiv e-prints, arXiv:2408.00843, doi: [10.48550/arXiv.2408.00843](https://doi.org/10.48550/arXiv.2408.00843)
- Ryan, R. E., Thorman, P. A., Yan, H., et al. 2011, ApJ, 739, 83, doi: [10.1088/0004-637X/739/2/83](https://doi.org/10.1088/0004-637X/739/2/83)
- Schechter, P. 1976, ApJ, 203, 297, doi: [10.1086/154079](https://doi.org/10.1086/154079)
- Schlafly, E. F., & Finkbeiner, D. P. 2011, ApJ, 737, 103, doi: [10.1088/0004-637X/737/2/103](https://doi.org/10.1088/0004-637X/737/2/103)
- Schlegel, D. J., Finkbeiner, D. P., & Davis, M. 1998, ApJ, 500, 525, doi: [10.1086/305772](https://doi.org/10.1086/305772)
- Schmidt, K. B., Treu, T., Brammer, G. B., et al. 2014, ApJL, 782, L36, doi: [10.1088/2041-8205/782/2/L36](https://doi.org/10.1088/2041-8205/782/2/L36)
- Schneider, A. C., Burgasser, A. J., Gerasimov, R., et al. 2020, ApJ, 898, 77, doi: [10.3847/1538-4357/ab9a40](https://doi.org/10.3847/1538-4357/ab9a40)
- Scholtz, J., Witten, C., Laporte, N., et al. 2023, arXiv e-prints, arXiv:2306.09142, doi: [10.48550/arXiv.2306.09142](https://doi.org/10.48550/arXiv.2306.09142)
- Schreiber, C., Labb  , I., Glazebrook, K., et al. 2018, A&A, 611, A22, doi: [10.1051/0004-6361/201731917](https://doi.org/10.1051/0004-6361/201731917)
- Setton, D. J., Verrico, M., Bezanson, R., et al. 2022, ApJ, 931, 51, doi: [10.3847/1538-4357/ac6096](https://doi.org/10.3847/1538-4357/ac6096)
- Somerville, R. S., Lee, K., Ferguson, H. C., et al. 2004, ApJL, 600, L171, doi: [10.1086/378628](https://doi.org/10.1086/378628)
- Stark, D. P., Ellis, R. S., Charlot, S., et al. 2017, MNRAS, 464, 469, doi: [10.1093/mnras/stw2233](https://doi.org/10.1093/mnras/stw2233)
- Stefanon, M., Labb  , I., Bouwens, R. J., et al. 2019, ApJ, 883, 99, doi: [10.3847/1538-4357/ab3792](https://doi.org/10.3847/1538-4357/ab3792)
- Steidel, C. C., Adelberger, K. L., Dickinson, M., et al. 1998, ApJ, 492, 428, doi: [10.1086/305073](https://doi.org/10.1086/305073)
- Tacchella, S., Bose, S., Conroy, C., Eisenstein, D. J., & Johnson, B. D. 2018, ApJ, 868, 92, doi: [10.3847/1538-4357/aae8e0](https://doi.org/10.3847/1538-4357/aae8e0)
- Tacchella, S., Eisenstein, D. J., Hainline, K., et al. 2023, ApJ, 952, 74, doi: [10.3847/1538-4357/acdbc6](https://doi.org/10.3847/1538-4357/acdbc6)
- Tanaka, M., Valentino, F., Toft, S., et al. 2019, ApJL, 885, L34, doi: [10.3847/2041-8213/ab4ff3](https://doi.org/10.3847/2041-8213/ab4ff3)
- Tanaka, M., Onodera, M., Shimakawa, R., et al. 2024, ApJ, 970, 59, doi: [10.3847/1538-4357/ad5316](https://doi.org/10.3847/1538-4357/ad5316)
- Tang, M., Stark, D. P., Chen, Z., et al. 2023, arXiv e-prints, arXiv:2301.07072, doi: [10.48550/arXiv.2301.07072](https://doi.org/10.48550/arXiv.2301.07072)
- Tilvi, V., Malhotra, S., Rhoads, J. E., et al. 2020, ApJL, 891, L10, doi: [10.3847/2041-8213/ab75ec](https://doi.org/10.3847/2041-8213/ab75ec)
- Trapp, A. C., & Furlanetto, S. R. 2020, MNRAS, 499, 2401, doi: [10.1093/mnras/staa2828](https://doi.org/10.1093/mnras/staa2828)
- Trapp, A. C., Furlanetto, S. R., & Davies, F. B. 2022, arXiv e-prints, arXiv:2210.06504, <https://arxiv.org/abs/2210.06504>

- Trenti, M., & Stiavelli, M. 2008, ApJ, 676, 767, doi: [10.1086/528674](https://doi.org/10.1086/528674)
- Trenti, M., Bradley, L. D., Stiavelli, M., et al. 2011, ApJL, 727, L39, doi: [10.1088/2041-8205/727/2/L39](https://doi.org/10.1088/2041-8205/727/2/L39)
- . 2012, ApJ, 746, 55, doi: [10.1088/0004-637X/746/1/55](https://doi.org/10.1088/0004-637X/746/1/55)
- Treu, T., Schmidt, K. B., Trenti, M., Bradley, L. D., & Stiavelli, M. 2013, ApJL, 775, L29, doi: [10.1088/2041-8205/775/1/L29](https://doi.org/10.1088/2041-8205/775/1/L29)
- Treu, T., Roberts-Borsani, G., Bradac, M., et al. 2022, ApJ, 935, 110, doi: [10.3847/1538-4357/ac8158](https://doi.org/10.3847/1538-4357/ac8158)
- Übler, H., Maiolino, R., Curtis-Lake, E., et al. 2023, A&A, 677, A145, doi: [10.1051/0004-6361/202346137](https://doi.org/10.1051/0004-6361/202346137)
- Valentino, F., Magdis, G. E., Daddi, E., et al. 2020, ApJ, 890, 24, doi: [10.3847/1538-4357/ab6603](https://doi.org/10.3847/1538-4357/ab6603)
- Valentino, F., Brammer, G., Gould, K. M. L., et al. 2023, ApJ, 947, 20, doi: [10.3847/1538-4357/acbefa](https://doi.org/10.3847/1538-4357/acbefa)
- van Dokkum, P. G. 2001, PASP, 113, 1420, doi: [10.1086/323894](https://doi.org/10.1086/323894)
- Vanderplas, J., Connolly, A., Ivezić, Ž., & Gray, A. 2012, in Conference on Intelligent Data Understanding (CIDU), 47 – 54, doi: [10.1109/CIDU.2012.6382200](https://doi.org/10.1109/CIDU.2012.6382200)
- Vulcani, B., Trenti, M., Calvi, V., et al. 2017, ApJ, 836, 239, doi: [10.3847/1538-4357/aa5caf](https://doi.org/10.3847/1538-4357/aa5caf)
- Vulcani, B., Treu, T., Calabro, A., et al. 2023, ApJL, 948, L15, doi: [10.3847/2041-8213/accbc4](https://doi.org/10.3847/2041-8213/accbc4)
- Wang, T., Sun, H., Zhou, L., et al. 2024, arXiv e-prints, arXiv:2403.02399, doi: [10.48550/arXiv.2403.02399](https://doi.org/10.48550/arXiv.2403.02399)
- Weaver, J. R., Davidzon, I., Toft, S., et al. 2022, arXiv e-prints, arXiv:2212.02512. <https://arxiv.org/abs/2212.02512>
- Weibel, A., de Graaff, A., Setton, D. J., et al. 2024, arXiv e-prints, arXiv:2409.03829, doi: [10.48550/arXiv.2409.03829](https://doi.org/10.48550/arXiv.2409.03829)
- Whitler, L., Endsley, R., Stark, D. P., et al. 2023, MNRAS, 519, 157, doi: [10.1093/mnras/stac3535](https://doi.org/10.1093/mnras/stac3535)
- Wilkins, S. M., Vijayan, A. P., Lovell, C. C., et al. 2022, MNRAS, doi: [10.1093/mnras/stac3280](https://doi.org/10.1093/mnras/stac3280)
- Williams, C. C., Curtis-Lake, E., Hainline, K. N., et al. 2018, ApJS, 236, 33, doi: [10.3847/1538-4365/aabccb](https://doi.org/10.3847/1538-4365/aabccb)
- Williams, C. C., Oesch, P. A., Weibel, A., et al. 2024, arXiv e-prints, arXiv:2410.01875, doi: [10.48550/arXiv.2410.01875](https://doi.org/10.48550/arXiv.2410.01875)
- Williams, R. J., Quadri, R. F., Franx, M., van Dokkum, P., & Labb  , I. 2009, ApJ, 691, 1879, doi: [10.1088/0004-637X/691/2/1879](https://doi.org/10.1088/0004-637X/691/2/1879)
- Willott, C. J., Desprez, G., Asada, Y., et al. 2024, ApJ, 966, 74, doi: [10.3847/1538-4357/ad35bc](https://doi.org/10.3847/1538-4357/ad35bc)
- Witten, C., McClymont, W., Laporte, N., et al. 2024, arXiv e-prints, arXiv:2407.07937, doi: [10.48550/arXiv.2407.07937](https://doi.org/10.48550/arXiv.2407.07937)
- Yan, H., Yan, L., Zamojski, M. A., et al. 2011, ApJL, 728, L22, doi: [10.1088/2041-8205/728/1/L22](https://doi.org/10.1088/2041-8205/728/1/L22)
- Yung, L. Y. A., Somerville, R. S., Finkelstein, S. L., Popping, G., & Dav  , R. 2018, ArXiv e-prints. <https://arxiv.org/abs/1803.09761>
- Zhang, Z., Jiang, L., Liu, W., & Ho, L. C. 2024, arXiv e-prints, arXiv:2411.02729, doi: [10.48550/arXiv.2411.02729](https://doi.org/10.48550/arXiv.2411.02729)